

UNIVERSITY OF CALIFORNIA  
Santa Barbara

Diversity and Equalization for MultiGigabit  
Millimeter Wave Communications over a Sparse  
Multipath Channel

A Dissertation submitted in partial satisfaction  
of the requirements for the degree of

Doctor of Philosophy

in

Electrical and Computer Engineering

by

Hong Zhang

Committee in Charge:

Professor Upamanyu Madhow, Chair

Professor Jerry Gibson

Professor Mark Rodwell

Professor John Shynk

December 2012

The Dissertation of  
Hong Zhang is approved:

---

Professor Jerry Gibson

---

Professor Mark Rodwell

---

Professor John Shynk

---

Professor Upamanyu Madhow, Committee Chairperson

December 2012

Diversity and Equalization for MultiGigabit Millimeter Wave Communications  
over a Sparse Multipath Channel

Copyright © 2012

by

Hong Zhang

## Acknowledgements

Over the last five years, Professor Madhow has been a great adviser for me in so many ways. First, I have learnt from him the importance of understanding the big picture before trying to solve a complex research problem in my research work. Second, Professor Madhow has always spent considerable time on our research problems and he usually gives sharp insights into our problems, which helped me significantly for my research work. Last but not least, he is not only a great professor but also a great person, from whom I have learned how to get along well in a collaborative environment.

I would like to thank my committee members: Professor Rodwell, Professor Gibson and Professor Shynk, for their thoughtful comments and feedback. Particularly, I would like to thank Professor Rodwell for his help with our collaborative work on the channel measurement using the 60 GHz prototype.

I feel lucky to have so many great labmates—Sumit, Jaspreet, Eric, Sriram, Sandeep, Francois, Dinesh, Aseem— to work with, from discussions with whom I have got lots of useful new ideas. I also would like to thank them for their feedback on my papers or my work. Besides the lab work, we have also had lunch together so many times in front of the beautiful Pacific ocean.

I would like to thank my husband Fei Peng for his unconditional love and support

as always. For my lovely son Justin, I would like to say thank you for being such a healthy and happy baby who brings me much happiness. My parents and my mother-in-law have supported me a lot by helping me take care of Justin. I would like to express my deep appreciation for them and I cannot have finished my Ph.D. work without their help.

For my daily life at Santa Barbara, I would like to thank many great friends. Thanks to my dear friends Molly and Steve for their care and help. Thanks to my friends– Jing, Jingning, Kejun, Yuli, Xiaohui, Shiyuan, Fei Guo and other friends– who have made my daily life enjoyable and wonderful.

# Curriculum Vitæ

## Hong Zhang

### Education

|               |  |
|---------------|--|
| December 2012 | Doctor of Philosophy, Electrical and Computer Engineering<br>University of California, Santa Barbara |
| December 2008 | Master of Science, Electrical and Computer Engineering<br>University of California, Santa Barbara    |
| March 2006    | Master of Science, Signal and Information Processing<br>Beijing Institute of Technology, China       |
| June 2003     | Bachelor of Science, Electrical Information Engineering<br>Wuhan University, China                   |

### Publications

#### Conferences

- H. Zhang, T. Chen, M. Ting, and X. Li, “Efficient design-specific worst case corner extraction for Integrated circuits”. *IEEE Design Automation Conference (DAC)*, July, 2009, California.
- H. Zhang, S. Venkateswaran and U. Madhow. “Channel Modeling and MIMO Capacity For Outdoor Millimeter Wave Links”. *IEEE Wireless Communications and Networking Conference*, April 2010, Sydney, Australia.
- H. Zhang, U. Madhow, “Statistical Modeling of Fading and Diversity for Outdoor 60 GHz Channels”. *International Workshop on mmWave Communications: from Circuits to Networks(mmCom10)*, Chicago, IL, Sept. 2010.
- E. Torkildson, H. Zhang, U. Madhow, “Channel Modeling for Millimeter Wave MIMO,” *Information Theory and Applications Workshop(ITA)*, San Diego, CA, Feb. 2010.
- H. Zhang, S. Venkateswaran and U. Madhow, “Analog Multitone with Interference Suppression: Relieving the ADC Bottleneck for Wideband 60 GHz Systems,” *IEEE Globecom*, to be appeared, Anaheim, CA, Dec. 2012.

#### Journals

- H. Zhang and U. Madhow. “Quasi-deterministic diversity for sparse multipath channels: design of robust, highly directional, outdoor 60 GHz links”, *IEEE Transactions on Wireless Communications (submitted)*

## Abstract

# Diversity and Equalization for MultiGigabit Millimeter Wave Communications over a Sparse Multipath Channel

Hong Zhang

We undertake a fundamental investigation of diversity and equalization over highly directional links in the millimeter(mm) wave band. Our focus is on outdoor links using the 60 GHz unlicensed spectrum. Such links could be used to form wireless mesh networks with multiGigabit data rates. **The use of directional transmission and reception contributes to a few strong paths which fall within the transmit and receive antenna beamwidths. We find that such *sparse* multipath channels require new design approaches relative to design of conventional wireless links in rich scattering environments.**

We investigate spatial and frequency diversity for such highly directional links for which the number of dominant paths is significantly smaller than for the scattering environments seen by omnidirectional links. While fading can still be severe, we observe that the channel statistics are very different from classical Rayleigh or Rician fading models, and are characterized by the variations in a small number of parameters characterizing the propagation geometry. While our findings are quite general, our specific focus is on modeling outdoor millimeter wave lamppost-to-

lamppost links in an urban environment (e.g., for multiGigabit mesh networks using 60 GHz unlicensed spectrum). We show that it is possible to design *quasi-deterministic* diversity strategies such that geometric configurations which result in destructive interference are unlikely. The rules of thumb regarding antenna spacing and bandwidth differ significantly from those for standard rich scattering models, and outage probabilities of the order of  $10^{-4}$  or less can be obtained with small link margins (a few dB) relative to a line-of-sight (LoS) link.

Commercial exploitation of such multiGigabit mesh network at 60 GHz band requires that we take advantage of the low-cost digital signal processing (DSP) made available by Moore's law. A key bottleneck, however, is the cost and power consumption of high-precision analog-to-digital converters (ADCs) at the multiGigabit rates of interest in this band. This makes it difficult, for example, to apply traditional DSP-based approaches to channel dispersion compensation such as time domain equalization or Orthogonal Frequency Division Multiplexing (OFDM), since these are predicated on the availability of full-rate, high-precision samples. We investigate the use of analog multitone for sidestepping the ADC bottleneck: transmissions are split into a number of subbands, each of which can be separately sampled at the receiver using a lower rate ADC. Given the large coherence bandwidth of the sparse multipath channels typical of such highly directional outdoor 60 GHz links that we consider, reliable performance requires spatial

diversity, in addition to the beamforming required to close the link. We therefore consider one transmit and two receive antenna arrays, each with  $4 \times 4$  elements. We find that exploiting spatial diversity completely by combining samples from both arrays is critical for combating fading and inter carrier interference.

# Contents

|  |            |
|--|------------|
| <b>Acknowledgements</b>  | <b>iv</b>  |
| <b>Curriculum Vitæ</b>   | <b>vi</b>  |
| <b>Abstract</b>  | <b>vii</b> |
| <b>List of Figures</b>   | <b>xii</b> |
| <b>List of Tables</b>  | <b>xiv</b> |
| <b>1 Introduction</b>  | <b>1</b>   |
| 1.1 Dissertation Overview . . . . .                              | 5          |
| 1.2 Contribution and Impact . . . . .                            | 9          |
| 1.3 Dissertation Outline . . . . .                               | 14         |
| <b>2 Channel Modeling for a Lamppost-based Link</b>              | <b>16</b>  |
| 2.1 Nominal Link Parameters . . . . .                            | 17         |
| 2.2 Ray-tracing Channel Model . . . . .                          | 19         |
| 2.2.1 Reflection Coefficients . . . . .                          | 20         |
| 2.2.2 Multi-ray Channel Model . . . . .                          | 23         |
| 2.3 Simplified Multi-ray Channel Model . . . . .                 | 25         |
| 2.3.1 Statistical Modeling . . . . .                             | 27         |
| <b>3 Spatial Diversity for Narrowband Channel</b>                | <b>28</b>  |
| 3.1 Sparse Multipath Fading . . . . .                            | 29         |
| 3.2 Deterministic Diversity for a Two-ray Model . . . . .        | 32         |
| 3.3 Quasi-deterministic Diversity for Multi-ray Models . . . . . | 37         |
| 3.3.1 Three-ray Channel Model . . . . .                          | 37         |

|          |  |           |
|----------|--|-----------|
| 3.3.2    | MIMO SNR Gains . . . . .                                   | 41        |
| 3.3.3    | Antenna Spacing . . . . .                                  | 42        |
| <b>4</b> | <b>Frequency Diversity for Wideband Channel</b>            | <b>46</b> |
| <b>5</b> | <b>Combined Frequency and Spatial Diversity</b>            | <b>50</b> |
| 5.1      | Outage Probability . . . . .                               | 51        |
| 5.2      | Robustness to Changes in Propagation Environment . . . . . | 53        |
| <b>6</b> | <b>Analog Multitone</b>                                    | <b>58</b> |
| 6.1      | Introduction . . . . .                                     | 58        |
| 6.2      | System Model . . . . .                                     | 63        |
| 6.2.1    | Link Budget and Channel Model . . . . .                    | 64        |
| 6.2.2    | Complex Baseband Model . . . . .                           | 67        |
| 6.3      | Equalization Schemes . . . . .                             | 70        |
| 6.4      | Simulation Results . . . . .                               | 76        |
| 6.4.1    | Selecting the Number of Subbands . . . . .                 | 77        |
| 6.4.2    | Design of Multiple Antenna Arrays . . . . .                | 81        |
| 6.4.3    | BER Performance . . . . .                                  | 83        |
| 6.5      | Summary . . . . .  | 88        |
| <b>7</b> | <b>Conclusions</b>   | <b>89</b> |
|          | <b>Bibliography</b>  | <b>91</b> |

# List of Figures

|     |  |    |
|-----|--|----|
| 1.1 | The unlicensed millimeter wave bandwidth allocation. . . . .   | 2  |
| 1.2 | Illustration of millimeter wave outdoor mesh network with nodes deployed on lampposts along a city street. . . . .   | 5  |
| 1.3 | Illustration of the necessity of directionality in millimeter wave band. . . . .   | 7  |
| 2.1 | The propagation geometry for a lamppost-to-lamppost link in an urban environment, including the LoS path and reflections from the ground and building walls (only single bounce reflections are shown in the figure for clarity.) . . . . .  | 17 |
| 3.1 | Path gain of a SISO system as a function of transmission range, using the six-ray channel model. . . . .   | 30 |
| 3.2 | A two-ray model with the LoS path and a single reflected path. . . . .   | 34 |
| 3.3 | Phasors corresponding to the normalized LoS path and reflected path. A fade beyond the link margin occurs if the relative phase of the reflected path falls within the shaded “danger zone” in the SISO system. . . . .  | 35 |
| 3.4 | A complete fade at both antennas happen with a three-ray model for $1 \times 2$ SIMO. For $\alpha_1 = \alpha_2 = 1$ , $\gamma_1 = 2\pi/3$ , and $\gamma_2 = 4\pi/3$ , we obtain $ 1 + e^{j(\pi-\phi_0)} + e^{j(\pi+\phi_0)}  = 0$ at the first receive antenna, and $ 1 + e^{j(\pi-\phi_0+2\pi/3)} + e^{j(\pi+\phi_0+4\pi/3)}  = 0$ at the second receive antenna. . . . . | 39 |
| 3.5 | Outage probabilities versus antenna spacing for different diversity strategies (5 dB link margin). . . . .   | 44 |
| 3.6 | Simulation results for spatial diversity. . . . .  | 45 |
| 5.1 | Outage probabilities for SISO and $1 \times 2$ SIMO links as a function of channel bandwidth. . . . .  | 53 |
| 5.2 | Probability of outage as a function of link range. . . . .   | 54 |

|      |  |    |
|------|--|----|
| 5.3  | Outage capacity for different reflection surfaces for spatial diversity, frequency diversity and combined diversity. . . . .   | 56 |
| 6.1  | Illustration of normalized channel impulse responses of a system of 2 GHz bandwidth at 60 GHz band with different number of subbands (The star marker denotes the ICI signal from the adjacent subband on the left). . . . . | 60 |
| 6.2  | Block diagram of the analog multitone system (only one of the two receive arrays is shown for simplicity). . . . .   | 62 |
| 6.3  | Illustration of the subband allocation. . . . .  | 68 |
| 6.4  | Block diagram of ISEL or JSEL scheme. . . . .  | 71 |
| 6.5  | Block diagram of ICOM or JCOM scheme. . . . .  | 72 |
| 6.6  | The CDF of the obtained SINR of the ISEL scheme with 4 and 8 subband channels for different antenna separations from $2\lambda$ to $8\lambda$ . . . .  | 76 |
| 6.7  | Illustration of normalized channel impulse responses for the two-ray channel model in a system with different numbers of subbands. . .   | 80 |
| 6.8  | Illustration of normalized channel impulse responses for the three-ray channel model in a system with different numbers of subbands. . .   | 81 |
| 6.9  | SINR as a function of equalizer taps per subband per antenna array for four schemes with 4 subbands and 8 subbands. . . . .  | 83 |
| 6.10 | BER as a function of $E_b/N_0$ (along the LoS path) for different schemes with both adaptive implementation and calculation using perfect channel knowledge. . . . .   | 85 |
| 6.11 | BER comparison between the ICOM scheme with Nyquist sampling and ISEL scheme with oversampling factors of 1, 2 and 4. (adp: adaptive implementation, th: calculation using perfect channel knowlege)                         | 86 |

# List of Tables

|     |   |    |
|-----|---|----|
| 5.1 | Required link margins (LM) to achieve $10^{-4}$ outage probability. | 54 |
|-----|---|----|

# Chapter 1

## Introduction

As the increasing popularity of smart phones and tablets, wireless data growth has led to significant spectrum deficit. One solution is to place many small cells to meet the demand of increasing wireless data rate; however, this leads to the need for a new generation of networks that support multiGigabit communications. Although optical fiber is a common method to provide such high speed communications, it is very costly and inconvenient to dig up roads to lay fibers especially in a metropolitan area. The 60 GHz band is considered to be a promising candidate for building such high speed, short range wireless networks for a number of reasons: it offers large swathes of unused bandwidth (bandwidth allocation is shown in Figure 1.1) and has a high spatial frequency reuse because of significant attenuation due to oxygen absorption [1].

Advances in silicon implementations of millimeter (mm) wave transceivers in recent years [2,3] have opened up the possibility of low-cost multiGigabit wireless

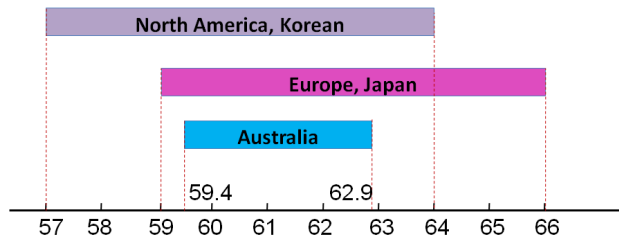


**Figure 1.1:** The unlicensed millimeter wave bandwidth allocation.

networks using several GHz of unlicensed spectrum at 60 GHz. While much of this interest has focused on indoor communication, with significant impetus from industry consortia such as the Wireless Gigabit Alliance [4] and standards such as IEEE 802.11ad [5]. Recent work [6] [7] shows that *outdoor* mesh networks based on short-range (100s of meters) 60 GHz links are a promising approach to providing a quickly deployable multiGigabit wireless backhaul (e.g. for picocellular networks or for “last-hop” links in a neighborhood). **In this thesis, we investigate space-time channel models for such 60 GHz wireless outdoor links, which include only a few strong paths induced by the use of highly directional antennas at both transmitter and receiver. For convenience, we term such a multipath channel that contains a few strong paths as the *sparse* multipath channel.** We employ ray tracing to show that such channels are qualitatively different from the Rayleigh or Rician fading typically encountered for omnidirectional links. While our observations regarding the effects of directionality are quite general, our focus is on modeling a

lamppost-to-lamppost millimeter (mm) wave link in an urban environment (shown in Figure 1.2), where the lampposts are typically lower than rooftops of the nearby buildings.

There is a significant literature on channel measurement, ray tracing, and statistical channel modeling for the 60 GHz channel, for both indoor [8–11] and outdoor [12–16] links. In both settings, ray tracing based channel models show good agreement with measurement results, indicating that diffraction effects can be neglected. A key difference from indoor channel modeling is that blockage, which occurs routinely due to obstacles such as furniture and humans indoors [17] [7], is less important for an outdoor link for a well-designed deployment. We ignore blockage resulting from seasonal foliage growth in our modeling in order to focus on the fundamentals of multipath fading.

Prior work on outdoor mm wave backhaul has considered hierarchical beamforming techniques [18] and the impact of ground movement and wind on the beam alignment [19] (the latter effects are actually quite negligible for mm wave links). To the best of our knowledge, however, this is the first work to conduct a fundamental investigation of diversity in such settings. This dissertation employs the ray tracing based modeling approach to provide analytical insights into design with both spatial and frequency diversity, validated by extensive simulations.

While we consider spatial diversity in near-LoS environments in this dissertation, we note that, for antenna spacings that are sufficiently large (relative to the carrier wavelength), it is also possible to obtain spatial multiplexing gains in near-LoS environments [20–22]. For the ranges and node form factors (which constrain the attainable antenna spacings) of interest in this work, however, spatial multiplexing gains are not attainable unless we decrease the carrier wavelength further (e.g., by pushing carrier frequencies beyond 100 GHz).

Note that a key bottleneck to implement such high speed wireless communications in the mm wave band is the cost and power consumption of high-precision analog-to-digital converters (ADCs). This makes it difficult, for example, to apply traditional DSP-based approaches to channel dispersion compensation such as time domain equalization or Orthogonal Frequency Division Multiplexing (OFDM) (due to the high peak-to-average power ratio (PAPR) problem). Therefore, we investigate the use of analog multitone for sidestepping the ADC bottleneck: transmissions are split into a number of subbands, each of which can be separately sampled at the receiver using a lower rate ADC. Novel equalizer schemes are proposed for such an analog multitone system achieving robust multiGigabit transmissions with a small number of subbands.

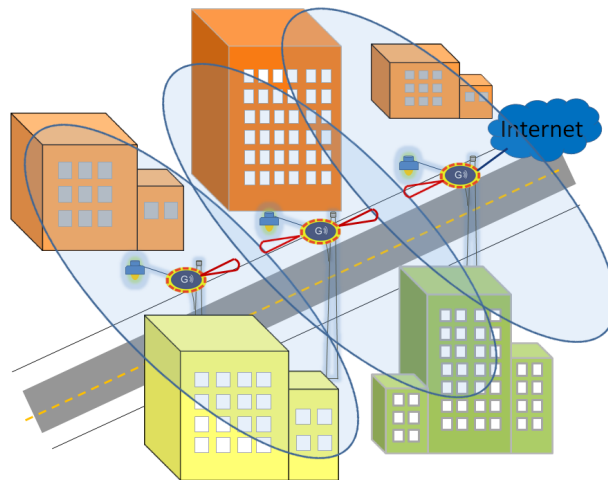


**Figure 1.2:** Illustration of millimeter wave outdoor mesh network with nodes deployed on lampposts along a city street.

## 1.1 Dissertation Overview

Figure 1.2 illustrates the envisioned 60 GHz outdoor wireless mesh network in an urban street environment, where the nodes are deployed on the top of lampposts. Such wireless networks, in conjunction with optical fiber for longer range communications, can provide an easily deployable broadband infrastructure. Moreover, such 60 GHz wireless mesh network can serve as a multiGigabit wireless backhaul network for small local area network (LAN) such as Femtocells or WiFi networks. In this thesis, we investigate the system design for this multiGigabit 60 GHz wireless network, focusing on the diversity and equalizer schemes based on the ray-tracing channel model.

The differences between mm wave and WiFi networks at 2.4 and 5 GHz stem from the order of magnitude difference in wavelength  $\lambda$  of the carrier used for transmission. Since free space propagation loss scales as  $\lambda^2$ , the propagation loss in mm-wave networks is 28 dB higher than the loss in WiFi networks (at 2.4 GHz). On the other hand, the antenna directivity scales as  $\lambda^{-2}$  for an antenna with a given aperture (corresponding to nodes with a fixed form factor). Therefore, using directional antennas at both the transmitter and the receiver leads to a net power scaling of  $\lambda^{-2}$ , which translates to an advantage of 28 dB for 60 GHz versus 2.4 GHz (shown in Figure 1.3). Since it is difficult to produce high transmit powers using low-cost silicon implementations, the use of directional transmission and reception is imperative at 60 GHz. Fortunately, the smaller wavelength also makes it possible to synthesize low-cost antenna arrays (e.g., implemented as patterns of metal on circuit board), which can then be electronically steered to provide adaptive yet highly directional links permitting a flexible deployment. From the point of view of channel modeling, the consequence of directionality is that the channel between the transmitter and receiver is dominated by a few paths which fall within the transmit and receive antenna beamwidths. This is fundamentally different from the much richer scattering environment for omnidirectional links at lower carrier frequencies.

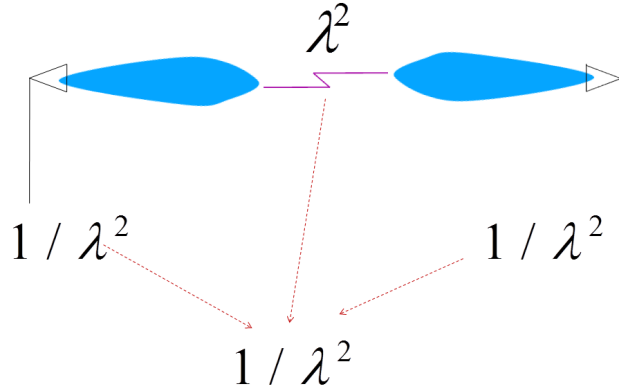


**Figure 1.3:** Illustration of the necessity of directionality in millimeter wave band.

We employ the ray-tracing channel model to investigate diversity schemes to provide robust link performance [23] [24] [25]. In order to develop fundamental insight, we first consider spatial diversity for a narrowband channel, then consider frequency diversity for a wideband channel, and then discuss combining the two strategies [26]. For both narrowband and wideband systems, we discover that, while standard multiple input multiple output (MIMO) diversity techniques apply, the underlying geometry and achievable performance are very different from that for rich scattering environments. Statistical channel models must be closely tied to the propagation geometry, and it is possible to devise diversity strategies that make the probability of geometric configurations causing destructive interference very unlikely, leading to deterministic or quasi-deterministic performance

guarantees (e.g., outage probabilities smaller than  $10^{-4}$  with link margins relative to an LoS link of the order of 1-5 dB). This is in contrast to the much larger link margins required for classical Rayleigh fading channels.

Time domain equalization and OFDM are popular approaches to combat channel dispersion commonly encountered in wideband wireless channels. However, both these approaches require a large dynamic range at the receiver or equivalently a high precision ADC. Multi-Gigabit links exacerbate this challenge by demanding a high sampling rate along with high precision from the ADCs. In order to avoid the burden of high cost and power consumption from such high performance ADCs, we investigate an Analog Multitone (AMT) scheme, where the signal bandwidth is split into a small number of sub-bands in the analog domain and each of the subbands is sampled at a relatively low sampling rate [27]. In order to fully utilize the spectrum, we don't allow guard bands between adjacent subbands, while each subband has some excess bandwidth to limit inter-symbol interference (ISI). We need to suppress the resultant inter-carrier interference (ICI) and any residual ISI at the receiver. We find that utilizing spatial diversity (employing linear equalization for samples from both arrays) is critical to combat ICI in addition to fading. Specifically, we consider a  $1 \times 2$  SIMO system with beamforming antenna pattern at both ends of the link. We investigate multiple schemes

by choosing to combine or select the antennas and to perform independent or joint equalization.

## 1.2 Contribution and Impact

In this section, we list our contributions and the impact of our research on exploring the 60 GHz band for wireless outdoor backhaul network, focusing on the sparse multipath channel modeling, spatial diversity, frequency diversity and the AMT scheme. For the first three parts, we consider fixed horn antennas pointing along the LoS, since our goal is to provide fundamental analytical insight into the nature of diversity with sparse multipath. For the AMT scheme, we consider the electronically beamsteered array to show the robustness of our design to variations of antenna type. Our main contributions are summarized as follows:

**Sparse Multipath Channel Modeling:** We model (in Chapter 2) a typical lamppost-to-lamppost 60 GHz link with three to six rays, consisting of the LoS path, the ground reflection, and bounces from buildings located at both sides of the street. Including the bounce from the nearest wall alone gives a three-ray model, while including both single bounces and double bounces from both sides of the street results in a six-ray model. The statistics of the channel are induced by statistical models for variations in lamppost heights and wall distances.

**Spatial Diversity:** We investigate different MIMO spatial diversity strategies for the narrowband system and we show that the *quasi-deterministic* diversity can be achieved via choosing the appropriate antenna spacing.

- We develop analytical insight (in Section 3.2) into the nature of fading and spatial diversity in sparse multipath by considering the simplest possible scenario of narrowband signaling over a two-ray channel (with the LoS path and a single reflected path). We observe that fading for a single-input single-output (SISO) link becomes severe beyond a certain range, but show that it is possible to provide *deterministic* spatial diversity. Specifically, we show that it is possible to space the antennas such that when one receive antenna sees a destructive fade, the other is *guaranteed* to see a constructive fade. This is fundamentally different from the *probabilistic diversity* in standard independent and identically distributed (i.i.d.) Rayleigh fading models, and implies that we can operate under significantly smaller link margins. For the propagation geometries of interest, the required spacing is several times the carrier wavelength (which is still compatible with compact node form factors for the small wavelengths of interest here).
- We show (in Section 3.3.3) that the qualitative observations regarding fading and spatial diversity for the two-ray model also hold for three- and six-ray

channel models, and for a variety of MIMO diversity schemes, including  $1 \times 2$ ,  $2 \times 1$  and  $2 \times 2$  systems. While deterministic guarantees can no longer be given, *quasi-deterministic* diversity is obtained using design prescriptions on antenna spacing obtained from analysis of the two-ray model: small outage probabilities (less than  $10^{-4}$ ) can be obtained with a link margin of 5 dB, which is far better than the achievable performance for i.i.d. Rayleigh fading for appropriately chosen spacings. However, antenna spacings that are too large destroy quasi-determinism by randomizing the relative phases of the paths at different antennas, and performance can revert to the probabilistic diversity typical of standard Rayleigh fading models.

**Frequency Diversity:** We provide analytical insight into when deterministic frequency diversity is possible for such a sparse multipath frequency selective wideband channel at 60 GHz band.

- We derive analytical insight into frequency diversity (in Chapter 4) using a three-ray channel model for a SISO link. Using the averaged power gain over the band as a metric, we show that *deterministic* frequency diversity is obtained, with less than a dB degradation with respect to a LoS link, when the bandwidth  $B$  is greater than the inverse of the *minimum* delay spread  $\tau_{min}$ , defined as the delay difference between the LoS path and the

closest other path. The condition  $B \geq \frac{1}{\tau_{min}}$  also yields quasi-deterministic frequency diversity for more complex six-ray models, with outage probabilities smaller than  $10^{-4}$  obtained with link margins of less than 0.5 dB relative to a LoS link. This is in contrast to rich scattering environments, in which the bandwidth requirements are loosely governed by the root mean squared (rms) delay spread, and where deterministic guarantees are typically not possible.

**Combined Diversity Scheme:** When the bandwidth  $B < \frac{1}{\tau_{min}}$ , we show that the combined diversity scheme provides quasi-deterministic diversity. We also illustrate the robustness of our design approach to variations in modeling, including significant changes in geometry and in link range, and variations in the model for reflection coefficients.

- We investigate combined spatial and frequency diversity for a  $1 \times 2$  SIMO link, and show that, when the antennas are spaced by several wavelengths (in Section 3.3.3) and the bandwidth  $B \geq \frac{1}{\tau_{min}}$ , then quasi-deterministic performance is obtained with *negative* link margins relative to our nominal SISO LoS link (e.g. when  $B = \frac{1}{\tau_{min}}$ ,  $10^{-4}$  outage probability at -2.8 dB margin relative to ideal SIMO, or 0.45 dB margin relative to ideal SISO).

- When the bandwidth  $B < \frac{1}{\tau_{min}}$ , then quasi-deterministic frequency diversity is no longer possible. However, combined frequency and spatial diversity yields quasi-deterministic performance in this regime (e.g.,  $10^{-4}$  outage at link margin of 0.9 dB when  $B \geq \frac{1}{8\tau_{min}}$ ). In the worst case when  $B \ll \frac{1}{\tau_{min}}$  (e.g., due to a drastic change from the nominal geometry), we can still provide quasi-deterministic performance by virtue of spatial diversity as in Chapter 3.

- We show that the quasi-deterministic diversity holds for variations in link ranges from 50 m to 400 m and variations in the model for reflection coefficients, using our proposed system design (appropriate antenna spacing and channel bandwidth) based on the link range of 200 m.

**Analog Multitone Scheme:** We investigate four linear equalization strategies for the AMT scheme in a  $1 \times 2$  SIMO system and illustrate that robust multiGigabit transmissions can be achieved with a small number of subbands.

- We derive an equivalent channel between the transmitter and the receivers (in a system with a  $4 \times 4$  transmit array, and two  $4 \times 4$  receive arrays) that accounts for the beamforming patterns and the physical multipath channel,

consisting of reflections off a nearby wall and the ground in addition to the LoS path.

- We split the transmissions into four or eight subbands and investigate four linear equalization strategies for demodulating each subband. These strategies are based on different combinations of the following choices: (a) Combine samples from both arrays optimally or choose samples from the array that sees the stronger channel in the subband and (b) Treat the interference from adjacent subbands as noise or exploit the structure of the interference from adjacent subbands.
- While we consider two receive arrays in order to provide spatial diversity, we find that the additional degrees of freedom provided by combining samples from both arrays provide much better interference suppression (avoiding error floors) than using only samples from the array which sees a stronger channel.

### 1.3 Dissertation Outline

The following chapters of the dissertation are organized as follows. Chapter 2 presents the ray-tracing channel modeling for the 60 GHz wireless backhaul

network in the urban city street environment with nodes deployed on the top of lampposts. To overcome fading stemming from the sparse multipath channel, we study (in Chapter 3) spatial diversity strategies for the narrowband system and investigate the impact of antenna separations on the link performance. In Chapter 4, we provide analytical insights into the achievable frequency diversity for the frequency selective wideband channel. In Chapter 5, we demonstrate the combined diversity scheme, combining frequency diversity and spatial diversity, provides *quasi-deterministic* performance over a broad set of scenarios. We propose novel equalization schemes for the Analog Multitone (AMT) system (in Chapter 6). Chapter 7 concludes this dissertation with a brief summary of contributions and open issues.

## Chapter 2

# Channel Modeling for a Lamppost-based Link

We now discuss the propagation geometry of the lamppost-based mm wave link, shown in Figure 2.1. The transmitter and receiver for our link are placed on top of lampposts, and can be either on the same side of the street, or on different sides of the street. The street is assumed to be well approximated as straight over the link ranges of interest, and to have buildings on both sides. The assumption of buildings *throughout* the street is pessimistic: in practice, the absence of tall buildings at street intersections might cause fewer reflected rays which would, in turn, be expected to lead to diminished fading. We assume that the building walls nearest to a lamppost are at distance  $r_{wall}$  from it and also assume the antenna is at distance  $r_{street}$  from the ground (these distances will subsequently be modeled as random in order to capture the effects of variations in the propagation geometry). The street width is denoted by  $S$ . The link range  $R$  is 100-200 m.

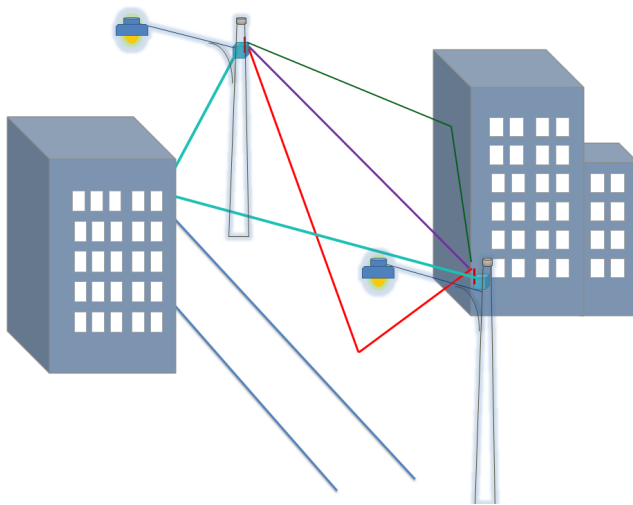


**Figure 2.1:** The propagation geometry for a lamppost-to-lamppost link in an urban environment, including the LoS path and reflections from the ground and building walls (only single bounce reflections are shown in the figure for clarity.)

## 2.1 Nominal Link Parameters

Before presenting the details of the channel model, it is helpful to get a feel for the nominal link parameters used for the numerical examples in this dissertation. Consider a 2 Gbps QPSK link, over a distance of 200 m, operating with a bandwidth of 1.5 GHz. For uncoded bit error rates (BERs) lower than  $10^{-9}$ , the required signal-to-noise ratio (SNR) is 14 dB (light coding can significantly reduce this requirement). We consider a vertically polarized antenna pattern at each end: a horn antenna [30] [31] with  $13^\circ$  vertical beamwidth and  $15^\circ$  horizontal beamwidth, corresponding to a directivity of 21.3 dBi, where the antenna beamwidth used in this dissertation is the half power beamwidth. We expect that

only few reflected paths are present due to the high directivity antenna gain, and would like to explore to what extent that affects the nature of fading and diversity. In practice, such antenna directivities might be realized using electronically steerable antenna arrays rather than a single horn, but our focus here is on providing fundamental insight into fading and diversity, hence we do not consider the additional gains (e.g., multipath suppression) that may be provided by transmit and receive beamforming. We note that our channel modeling approach is robust to the specific antenna pattern, as long as the directivities are high enough to reject reflections beyond second order. For example, we show in Chapter 6 that the same channel modeling approach is also suitable for a link with beamforming antenna arrays at both ends.

Assuming that the oxygen absorption loss is 16 dB/km, we find that, for a link margin of 5 dB and receiver noise figure of 3 dB, the required transmit power is 14.4 dBm. The effective isotropic radiated power (EIRP) is therefore 35.7 dBm, which is smaller than the FCC limit of 40 dBm average EIRP [32]. While we have not budgeted for rain, which can further increase the attenuation, we note that a relatively modest increase in the transmit power can handle fairly heavy rain. For example, 56.4 mm/hour of rain causing 20 dB/km additional attenuation [33] requires adding 4 dB to the link budget at 200 m range, which still fits within the FCC limit. Note also that implementation of a directive transmit antenna as an

electronically steerable array implies that the power fed into an individual element could be realized by low-cost silicon implementations (e.g., 14 dBm net transmit power can be realized using an 8-element antenna array with each individual antenna element fed by a CMOS 5 dBm power amplifier [34]).

## 2.2 Ray-tracing Channel Model

Geometrical optics based ray tracing provides a low-complexity approximation for characterizing the propagation of electromagnetic waves when the scatterers are significantly larger than the wavelength, and their distances from the transmitter and receiver are large compared to the wavelength. Given the small wavelengths of interest here (5 mm at 60 GHz), these conditions are certainly satisfied. Moreover, many prior measurement campaigns have confirmed the accuracy of ray tracing for 60 GHz channel characterization [10] [11] [16]. Diffraction effects can be neglected at 60 GHz [10] because of the small wavelength, hence we focus on characterizing the superposition of the LoS component, together with reflections from street and building surfaces.

We consider a reflective surface with complex dielectric constant  $\epsilon_c = \epsilon_r - j\epsilon_r \tan(\delta)$ , where  $\epsilon_r$  denotes the relative dielectric constant and  $\tan(\delta)$  denotes the loss tangent. Unless specified otherwise, our simulations employ Fresnel Reflec-

tion Coefficients [35] (for a thick specimen with high loss tangent), and model reflecting surfaces as smooth and infinite (e.g., smooth wood for building surfaces and smooth concrete for the street). This is a worst-case model which leads to stronger reflected paths and more severe fading. We assume that building walls are made of wood with relative complex dielectric constant  $\epsilon_c = 1.5 - 0.01j$  [36], and that the street surface is concrete with  $\epsilon_c = 6.5 - 0.126j$  [37]. We also show the robustness of our design approach to variations of reflecting surfaces in Chapter 5, where we consider the multilayer reflection coefficients [38] (for a thin specimen with low loss tangent) and the rough surfaces accounting for the scattering loss. For completeness, we provide a description of standard computations of reflection coefficients as follows.

### 2.2.1 Reflection Coefficients

**Fresnel Reflection Coefficients** [35]: Consider electromagnetic waves impinging on a vacuum-material interface that is smooth, infinite, and thick with high loss tangent. When the polarization is perpendicular to the plane of incidence, the reflection coefficient is given by:

$$R_{\perp}(\theta_i) = \frac{E_{\perp,r}(\theta, i)}{E_{\perp,i}(\theta, i)} = \frac{\cos \theta_i - \sqrt{\mu' \epsilon_r - \sin^2 \theta_i}}{\cos \theta_i + \sqrt{\mu' \epsilon_r - \sin^2 \theta_i}} \quad (2.1)$$

When the polarization is parallel to the plane of incidence, the reflection coefficient is given by:

$$R_{\parallel}(\theta_i) = \frac{E_{\parallel,r}(\theta, i)}{E_{\parallel,i}(\theta, i)} = \frac{\mu' \epsilon_r \cos \theta_i - \sqrt{\mu' \epsilon_r - \sin^2 \theta_i}}{\mu' \epsilon_r \cos \theta_i + \sqrt{\mu' \epsilon_r - \sin^2 \theta_i}} \quad (2.2)$$

where  $\theta_i = \pi/2 - \theta_g$  is the angle of incidence ( $\theta_g$  is the grazing angle, shown in Figure 3.2), and the *relative complex dielectric constant*  $\epsilon_r$  for the material is given by  $\epsilon_r = \epsilon' - j \frac{\sigma}{2\pi f \epsilon_0}$ , with  $\epsilon'$  denoting relative dielectric constant,  $\mu'$  relative permeability,  $\sigma$  conductivity and  $\epsilon_0 = 8.854 \times 10^{-12} AS/Vm$ . We assume vertical polarization at both ends, so that the wall and ground reflection coefficients are given by  $R_{\perp}$  and  $R_{\parallel}$ , respectively.

**Multilayer Reflection Coefficients:** For a thin specimen with small loss tangent, the multiple reflections departing from the bottom surface of the slab cannot be neglected. In this case, the multilayer reflection coefficient matches well with the measurement results. The coefficient is equal to the sum of the Fresnel reflection coefficient (directly reflection from the impinging wave) and all the consecutive reflections caused by the transmissions and reflections inside the slab. This multilayer reflection model is given by [36]:

$$M = R - (1 - R^2) \frac{R e^{-j \frac{2\pi}{\lambda} \sqrt{\epsilon_r} e^{-\alpha l_s} e^{-j \frac{2\pi}{\lambda} l_d} \sin(\theta_i)}}{1 - R^2 e^{-j \frac{2\pi}{\lambda} \sqrt{\epsilon_r} e^{-\alpha l_s} e^{-j \frac{2\pi}{\lambda} l_d} \sin(\theta_i)}} \quad (2.3)$$

The attenuation coefficient inside the slab is given by  $\alpha = \frac{w \tan(\delta)}{2} \sqrt{\mu_0 \epsilon_r \epsilon_0}$ , with loss tangent  $\tan \delta = 60\sigma\lambda/\epsilon_r$ . The propagation path length inside the slab  $l_s$  is

given by:  $l_s = \frac{2d_{thk}}{\sqrt{1 - \frac{\sin^2(\theta_i)}{\epsilon_r}}}$ , and  $l_d$  represents the path length difference of two adjacent departing reflections:  $l_d = \frac{2d_{thk}}{\sqrt{\frac{\epsilon_r}{\sin^2(\theta_i)} - 1}}$ . Detailed measurement results from [38] show that the multilayer reflection model is suitable for most indoor building materials such as plasterboard or wooden panel, while Fresnel reflection coefficients are suitable for some of the outdoor building materials such as concrete or granite. We include some simulations (in Chapter 5) for multilayer models to demonstrate that our fundamental observations on the nature of sparse multipath are insensitive to variations in our modeling of reflection coefficients.

**Exponential Loss for Rough Surfaces:** As a rule of thumb (termed the Rayleigh criterion [38] for smoothness), the reflective surface is considered to be smooth if the standard deviation of surface roughness satisfies the following condition:  $\sigma_h < \frac{\lambda}{8 \cos \theta_i}$ . On the other hand, when  $\sigma_h > \frac{\lambda}{8 \cos \theta_i}$ , the surface is considered to be rough, and diffusive reflection is no longer negligible compared to the specular reflection. The reflection coefficient can be adjusted to account for additional scattering loss as follows [38]:

$$A = F e^{-\frac{1}{2} \left( \frac{4\pi\sigma_h \cos \theta_i}{\lambda} \right)^2}, \quad (2.4)$$

where  $F$  is the Fresnel reflection coefficient or the multilayer reflection coefficient depending on the thickness and the loss tangent of the specimen.

## 2.2.2 Multi-ray Channel Model

Using ray tracing, the complex baseband channel impulse response is given by [39]

$$h(t) = \frac{\lambda}{4\pi} \left( \frac{\sqrt{G}\delta(t)e^{-K_p R/2 - j2\pi R/\lambda}}{R} + \sum_{i=1}^{N_r-1} \frac{A_i \sqrt{G_i} \delta(t - \tau_i) e^{-K_p R_i/2 - j2\pi R_i/\lambda}}{R_i} \right) \quad (2.5)$$

where  $N_r$  is the number of rays (including the LoS and the reflected rays);  $G$  and  $G_i$  are the *products* of the transmit and receive antenna power patterns for the LoS component and the reflected components respectively;  $K_p$  is the coefficient for exponential attenuation, which equals  $0.0016 \log_e 10$  for oxygen absorption of 16 dB/km at 60 GHz (with additional attenuation due to rain, if present);  $R$  is the LoS path length, or range;  $R_i$  is the length of the  $i$ th reflected path;  $A_i$  is the reflection coefficient on the  $i$ th path; and  $\tau_i = (R_i - R)/c$  is the delay of the  $i$ th reflected ray relative to the LoS path.

**Relative channel impulse response:** We can simplify the notation by expressing this gain relative to that of an ideal LoS link with no reflections. This *relative channel impulse response* is then given by

$$h_r(t) = \delta(t) + \sum_{i=1}^{N_r-1} \frac{R}{R_i} \sqrt{\frac{G_i}{G}} A_i \delta(t - \tau_i) e^{-K_p \Delta R_i/2 - j2\pi \Delta R_i/\lambda} \quad (2.6)$$

where  $\Delta R_i = R_i - R$  is the relative path length of the  $i$ th reflected path.

**Sparse Multipath:** For the geometries and directivities that we consider, we observe that only reflections from surfaces at distances less than 13.2 m horizontally or 11.4 m vertically fall within the antenna beamwidth, assuming that the transmission range of interest is 200 m. For example, for a four-lane city street (with a street width of about 12 m) with antenna heights lower than 8 m and wall distances larger than 4 m, only the reflected paths from the ground and from the near wall, together with the LoS path, fall within the antenna beamwidth, if both transmit and receive antennas are pointing along the LoS. This results in a *sparse multipath* channel with only three rays. Since the antenna beamwidth we consider is the half-power beamwidth, which corresponds to a soft cutoff, we may also wish to account for attenuated rays outside the beamwidth. For example, we may augment our channel model to six rays, including the LoS path, the ground reflection, and first and second order reflections from building walls on both sides of the road. Here, the *order* of a reflected ray is defined as the number of reflections the ray undergoes before reception. While we choose to employ the six-ray model for accuracy in modeling and simulation, we turn to the three-ray model (and even to a two-ray model) to provide fundamental insight. We shall see that such analysis provide good design rules of thumb for the more detailed six-ray model, since the additional rays have small enough amplitudes that they have a minor effect on performance.

## 2.3 Simplified Multi-ray Channel Model

In order to derive analytical insight, we can further simplify the channel model (2.6) by noting that changes in the environmental geometry of the order of wavelengths (only 5 mm at 60 GHz) causes order of  $2\pi$  variation in the phase of the reflected ray (relative to the LoS ray). Therefore, it is reasonable to model the relative phase  $\phi_i$  of the  $i$ th reflected ray with respect to the LoS as independent and uniform over  $[0, 2\pi]$  for different  $i$ . Further, denoting the relative channel gain of the  $i$ th reflected ray to be  $\alpha_i = \frac{R}{R_i} \sqrt{\frac{G_i}{G}} A_i e^{-K_p \Delta R_i / 2}$ , we define the *simplified multi-ray channel model* of a SISO link as follows:

$$h_r(t) = \delta(t) + \sum_{i=1}^{N_r-1} \alpha_i e^{-j\phi_i} \delta(t - \tau_i) \quad (2.7)$$

where  $N_r$  denotes the number of rays, and  $\alpha_i$  is the normalized amplitude of the  $i$ th reflected ray. For the narrowband channel model, the corresponding normalized complex gain is given by:

$$h_r^{nb} = 1 + \sum_{i=1}^{N_r-1} \alpha_i e^{-j\phi_i} \quad (2.8)$$

**MIMO link:** We now extend the simplified multi-ray channel model to an  $N \times M$  MIMO link. We first show that the phase differences between the LoS paths between different antenna pairs can be neglected, so that we can focus on geometric modeling of the differences in the relative phases of the reflected paths for differ-

ent antenna pairs. The phase difference between the LoS path from the transmit element  $n$  to receive element  $m$  and the LoS path from transmit element  $n$  to receive element  $n$  is given by:  $\Delta\phi_{LoS} = \frac{2\pi}{\lambda}(\sqrt{R^2 + (|m-n|d)^2} - R) \approx \frac{2\pi(|m-n|d)^2}{2\lambda R}$  (for  $d \ll R$ ). For nominal parameters  $R = 200$  m,  $d = 5\lambda$  and  $m - n = 1$ , we have  $\Delta\phi_{LoS} = 0.002$ , which is small enough to be neglected. Further, the amplitudes and propagation delays of the LoS path  $\alpha_i(m, n)$  and  $\tau_i(m, n)$  are close to  $\alpha_i(1, 1)$  and  $\tau_i(1, 1)$ , respectively.

Therefore, the channel impulse response between transmit element  $n$  and receive element  $m$  is given by:

$$h_r(m, n) = \delta(t) + \sum_{i=1}^{N_r-1} \alpha_i \delta(t - \tau_i) e^{-j(\phi_i + \gamma_i(m, n))} \quad (2.9)$$

where  $\gamma_i(m, n)$  denotes the additional phase offset for the  $i$ th reflected path between the  $n$ th transmit element and the  $m$ th receive element. Setting  $\gamma_i(1, 1) = 0$  as reference, we have  $\gamma_i(m, n) = 2\pi \frac{l_i(m, n) - l_i(1, 1)}{\lambda}$ , where  $l_i(m, n)$  denotes the path length of the  $i$ th reflected ray from  $n$ th transmit antenna to  $m$ th receive antenna. For a narrowband channel, neglecting the delay spread  $\tau_i$ , we can further simplify the expression for the normalized complex channel gains as follows:

$$h_r^{nb}(m, n) = 1 + \sum_{i=1}^{N_r-1} \alpha_i e^{-j(\phi_i + \gamma_i(m, n))} \quad (2.10)$$

We employ these simplified models to investigate fading and spatial diversity for a narrowband link (in Chapter 3), and frequency diversity for a wideband link in Chapter 4.

### 2.3.1 Statistical Modeling

Antenna heights and wall distances could vary significantly across different network deployments, or even within a given deployment. Furthermore, some variation (on the order of a few centimeters) in the positioning of antennas is inevitable. Due to the small carrier wavelength, even small changes in the propagation geometry can significantly affect the channel coefficients and the resulting multipath fading. In order to investigate such phenomena systematically and to evaluate the robustness of the diversity strategies that we explore, we introduce a statistical model in which some of the key propagation parameters are modeled as random variables. In particular, unless specified otherwise, we model the antenna height  $r_{street}$  as a uniformly distributed random variable over the interval [5m,8m], and the distance to the near wall  $r_{wall}$  as uniformly distributed over [4m,20m]. The preceding ranges are chosen so that the contributions from the reflected rays are significant, fixing, for simplicity, the nominal transmission range  $R = 200$  m and nominal street width  $S = 12$  m.

## Chapter 3

# Spatial Diversity for Narrowband Channel

We show that severe fades occur in our geometry of interest, because the strength of one or more of the reflected paths is comparable to that of the LoS path for the glancing incidence that occurs at the transmission range of interest. In addition, the fades can vary significantly with the unavoidable changes on the order of centimeters (several wavelengths). The measurement results in [40] verify our simulation results by showing the presence of significant fading.

We begin by investigating spatial diversity for a narrowband link as a means of overcoming fading. We first consider a two-ray channel model to develop insight and show that deterministic diversity is guaranteed in a  $1 \times 2$  SIMO system with appropriate antenna spacing. Further, we show that, although deterministic diversity is not attainable for the three-ray channel model or the general six-ray channel model, *quasi-deterministic* diversity can be achieved by choosing the

appropriate antenna spacing, where *quasi-deterministic* diversity means that a small outage probability (below  $10^{-4}$ ) relative to the LoS link can be achieved given a small link margin.

### 3.1 Sparse Multipath Fading

In this section, we consider the simplified multi-ray channel model as in (2.8) for the narrowband SISO system. We show that the severe fades are present and that the fades can vary significantly with small changes on the order of centimeters.

**Path gain and fading:** The fading relative to an idealized LoS link is given by  $|h_r^{nb}|^2$  as in (2.8), while the propagation gain as a function of range is given by the propagation gain for the LoS path (using the Friis formula for free space propagation) times the fading gain:  $g(R) = G(\frac{\lambda}{4\pi R})^2 e^{-K_p R} |h_r^{nb}|^2$ .

**Grazing angle:** The grazing angle between the incoming/outgoing ray and the reflecting surface (which is  $90^\circ$  minus the angle of incidence) is given by:  $\theta_g = \tan^{-1} \frac{2r}{R} \approx \frac{2r}{R}$ . For  $r = 5$  m,  $R = 200$  m, we obtain  $\theta_g = 2.86^\circ$ . Reflection with a small grazing angle is termed *glancing incidence*, and such reflection creates a  $180^\circ$  phase shift and results in relatively small attenuation.

**Critical range:** First, we note that the possibility of fading occurs only when the reflected path falls within the antenna beamwidth. The angle of arrival/departure

of the reflected path relative to the LoS is given by:  $\theta_a = \tan^{-1} \frac{2r}{R} \approx \frac{2r}{R}$ , for  $r \ll R$ . The reflected path falls within the beamwidth if  $\theta_a \leq \theta_{bw}/2$ , where the HPBW (half-power beamwidth) of the antenna is represented by an angular interval  $[-\theta_{bw}/2, \theta_{bw}/2]$  around the LoS path. This happens if the range exceeds a critical range  $R_c$  given by:

$$R_c \approx \frac{4r}{\theta_{bw}} \quad (3.1)$$

For example, for  $r = 5$  m and  $\theta_{bw} = 20^\circ$ , we obtain  $R_c \approx 57$  m.

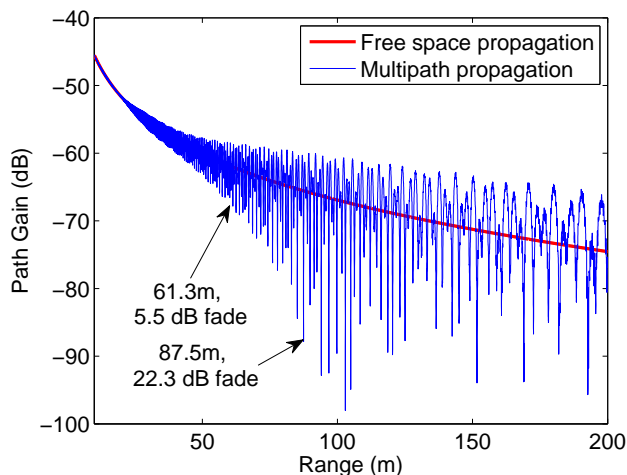


**Figure 3.1:** Path gain of a SISO system as a function of transmission range, using the six-ray channel model.

Figure 3.1 shows the variation of the propagation gain (in dB) as a function of range (transmitter and receiver located on the same side of the street), with the following parameters: wall distances at each side  $r_{wall} = 4$  m, antenna heights at each side  $r_{street} = 5$  m, street width  $S = 12$  m and transmission range up to

$R = 200$  m. The full-width half-max (FWHM) beamwidths for the antenna are  $15^\circ$  horizontal  $13^\circ$  vertical, and we plug these as  $\theta_{bw}$  in (3.1) to obtain the critical ranges for  $r_{wall}$  and  $r_{street}$  as 61 m and 88 m, respectively. Furthermore, when a single reflected ray gets into the FWHM beam, then it experiences a power attenuation of 3 dB at each end, corresponding to an amplitude attenuation of 3 dB relative to the LoS. Assuming grazing incidence, this corresponds to  $\alpha = 0.5$ , which gives a worst-case fade of  $20 \log_{10}(1 - \alpha) = 6$  dB. Indeed, Figure 3.1 shows that fades about 5.5 dB (relative to the free space benchmark) occur at the first critical range of 61.3 m. When more than one strong ray gets into the beam, as happens at the second critical range of 88 m, we expect deeper fades (the worst-case amplitude due to destructive interference can now be close to zero), and we do see fades deeper than 20 dB at 88 m. Of course, the horn antenna beam patterns let in attenuated versions of reflected rays at larger angles of arrival than those used for computing the critical ranges, hence we see the worst-case fades gradually increasing as the range increases, rather than just seeing sharp increases at the critical ranges (e.g., shallow fades happen even at ranges as small as 30 m).

**Sensitivity to changes in geometry:** Due to the small wavelength at the 60 GHz band, we expect fades to be extremely sensitive to small perturbations in geometry, and indeed, we find this to be the case even for the more detailed models we are now considering. For example, consider the six-ray channel model, fixing

$r_{wall} = 15.36$  m, the path gain for  $r_{street} = 5.01$  m is 0.1 dB smaller than the free space benchmark, but when we lower the antenna height 10 cm to  $r_{street} = 5$  m, the path gain drops to 38.9 dB below the free space benchmark!

## 3.2 Deterministic Diversity for a Two-ray Model

We consider the two-ray model depicted in Figure 3.2 to provide analytical insight, considering first a  $1 \times 1$  system to characterize fading, and then a  $1 \times 2$  system to understand diversity. Similarly as the simplified multi-ray channel model, the two-ray models for the SISO and SIMO system are given as below.

**SISO channel model:** For our  $1 \times 1$  system, the channel is modeled as:

$$h = 1 - \alpha e^{-j\phi}, \quad (3.2)$$

where the first term corresponds to the LoS ray, and  $\alpha > 0$  is the amplitude of the reflected ray relative to the LoS,  $\phi = 2\pi\ell_1$  is the received phase of the reflected ray relative to the LoS ray due to the path length difference. Since we model  $\phi$  as uniform over  $[0, 2\pi]$ , the negative sign in (3.2) makes no difference to the statistics of  $h$ , and is put in simply for notational convenience in later computations. However, it can be interpreted as modeling the approximately  $180^\circ$  phase shift produced by the glancing incidence.

**SIMO channel model:** We consider the  $1 \times 2$  SIMO system depicted in Figure 3.2(b), where we shall see that the distance  $d$  between the two receive antennas needs to be several multiples of  $\lambda$  to provide diversity. The channel gains from the transmit antenna to the two receive antennas can be modeled as follows:

$$h_1 = 1 - \alpha e^{-j\phi}, \quad h_2 = 1 - \alpha e^{-j(\phi+\gamma)} \quad (3.3)$$

where the phase difference between the two reflected paths is given by

$$\gamma \approx \frac{4\pi r d}{R\lambda}, \quad (3.4)$$

which is obtained based on the path length difference analysis discussed as follows. The path length difference between the reflected paths from the transmitter to the two receive antennas is given by

$$\Delta L_{reflected} = \sqrt{R^2 + (2r + d)^2} - \sqrt{R^2 + (2r)^2} \approx \frac{2rd}{R} \quad (3.5)$$

assuming that  $d \ll r \ll R$ . We would like this to be comparable to a carrier wavelength, in order to ensure that there is enough phase difference between the reflected paths to the two different receive antennas to provide diversity.

While we are interested in maximizing the gains from receive diversity via maximal ratio combining, it is easier to illustrate the concept of deterministic diversity for selection diversity. In particular, we now show that, corresponding to a nominal range for the propagation geometry parameters ( $r$  and  $R$ ), there

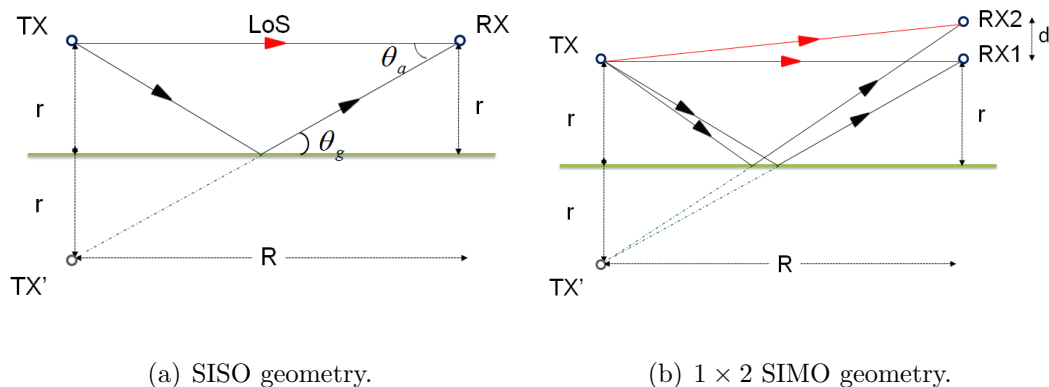


**Figure 3.2:** A two-ray model with the LoS path and a single reflected path.

is a range of choices for antenna spacing such that, when one of the receive antennas sees destructive interference, the other is *guaranteed* to see constructive interference.

**Deterministic diversity:** We wish to provide the deterministic guarantee that  $\max\{|h_1|, |h_2|\} \geq \beta$ , where  $\beta \leq 1$ . This corresponds to a link margin of  $20 \log_{10} \frac{1}{\beta}$  dB relative to our reference, which is a LoS SISO channel. For example, a link margin of 5 dB corresponds to  $\beta = 0.5623$ , while a link margin of 0 dB corresponds to  $\beta = 1$ . Since the worst-case channel gain in the SISO system is  $1 - \alpha$ , we assume  $\beta > 1 - \alpha$ ; that is, we cannot attain the desired link quality in a SISO system.

Now, suppose that  $|h_1| < \beta$ . From Figure 3.3, we see that this implies that  $|\phi| \leq \phi_0$ , where

$$\phi_0 = \cos^{-1} \left( \frac{1 + \alpha^2 - \beta^2}{2\alpha} \right) \quad (3.6)$$

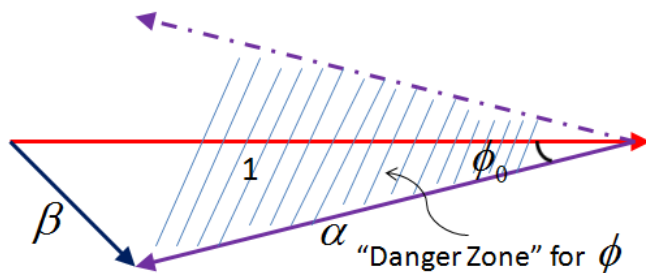


**Figure 3.3:** Phasors corresponding to the normalized LoS path and reflected path. A fade beyond the link margin occurs if the relative phase of the reflected path falls within the shaded “danger zone” in the SISO system.

That is, an unacceptable fade on antenna 1 implies that  $\phi \in [-\phi_0, \phi_0]$ . The probability of  $\phi$  falling in this “danger zone” (depicted in Figure 3.3) is given by

$$P[\text{fade in SISO system}] = \phi_0/\pi \quad (3.7)$$

For example, for  $R = 200$  m,  $r = 5$  m,  $\alpha = 0.95$ , we obtain  $\phi_0 = 0.58$  radians for a link margin of 5 dB (i.e.,  $\beta = 0.5623$ ), and  $\phi_0 = 1.08$  radians for a link margin of 0 dB ( $\beta = 1$ ). The corresponding probability of a fade in the SISO system is 18.55% for a link margin of 5 dB, and 34.24% for a link margin of 0 dB.

To provide deterministic diversity, the additional phase change  $\gamma$  for the second antenna must eject us from the danger zone in Figure 3.3. That is, if  $\phi \in [-\phi_0, \phi_0]$ , then we need  $\phi + \gamma \notin [-\phi_0, \phi_0]$ . This requires that  $|\gamma| \geq 2\phi_0$  to get us out of the danger zone. However, we also need that  $|\gamma|$  be small enough that we do not get back into this zone, which corresponds to the condition  $|\gamma| \leq 2\pi - 2\phi_0$ . Using (3.4), we obtain that the corresponding range for the normalized antenna spacing

is given by

$$\frac{\phi_0 R}{\pi 2r} \leq \frac{d}{\lambda} \leq \left(1 - \frac{\phi_0}{\pi}\right) \frac{R}{2r} \quad (3.8)$$

which evaluates to

$$\begin{aligned} 3.71 \leq \frac{d}{\lambda} \leq 16.29 & \quad \mathbf{5 \text{ dB link margin}} \\ 6.84 \leq \frac{d}{\lambda} \leq 13.15 & \quad \mathbf{0 \text{ dB link margin}} \end{aligned} \quad (3.9)$$

for the examples we have been considering. We observe that, even though SISO performance is unacceptable, SIMO performance can be *guaranteed* to be as good as that without fading (i.e, with 0 dB link margin) if we choose the antenna spacing appropriately. This is fundamentally different from the probabilistic approach to fading that must be adopted for rich scattering. Another key observation is that too large an antenna spacing is not desirable, as shown by the upper bounds in (3.8) and (3.9). In particular, for the two-ray model, changing  $\frac{d}{\lambda}$  by  $\frac{R}{2r}$  leads to a  $2\pi$  change in  $\gamma$ , so that there is a periodicity in performance as a function of  $\frac{d}{\lambda}$ . Of course, there is enough leeway in the preceding design prescriptions to allow for significant variations around the nominal link distance  $R$  without falling into this undesirable regime.

We now show that such properties, while not satisfied exactly, do hold qualitatively even in more complex environments, so that the two-ray analysis can be used to obtain design guidelines for more general sparse multipath settings.

## 3.3 Quasi-deterministic Diversity for Multi-ray Models

We first show, via a simple example, that deterministic diversity cannot be provided for even a three-ray model. However, we then show via simulations for a six-ray model that *quasi-deterministic* diversity can be achieved for more complex models, using the rules of thumb for antenna spacing derived from the two-ray model.

### 3.3.1 Three-ray Channel Model

Consider a three-ray channel model, including the LoS ray, the reflected ray from the nearest wall and the reflected ray from the ground. From the previous discussion, we show that diversity can be provided by spacing antennas so that they are at slightly different distances from the reflecting surface. Since we wish to provide diversity against wall reflections as well as street reflections, we must now offset antennas in both the horizontal and vertical directions. For simplicity, assume that the distances from the wall and street fall within the same range, which motivates offsetting the receive antennas from each other by the same amount  $d$  in each direction. Specializing (2.7) as we did for the two-ray model, the channel gain from the transmitter to the two receivers for the three-ray channel model is

given by:

$$\begin{aligned} h_1 &= 1 - \alpha_1 e^{-j\phi_1} - \alpha_2 e^{-j\phi_2}, \\ h_2 &= 1 - \alpha_1 e^{-j(\phi_1+\gamma_1)} - \alpha_2 e^{-j(\phi_2+\gamma_2)}. \end{aligned} \tag{3.10}$$

Define the outage probability of the SNR gain relative to the LoS path with a link margin of 0 dB as:  $P[\eta < 1]$ , where we define the SNR gain relative to a LoS link as  $\eta = |h_1|^2 + |h_2|^2$ , obtained using maximal ratio combining (MRC) at the receiver. The outage probability is defined as  $P[\eta < \beta^2]$ , where  $20 \log_{10} \frac{1}{\beta}$  dB is the link margin, as before.

We now observe that, unlike for the two-ray model, deterministic diversity is not possible. The example in Figure 3.4 illustrates that it is possible for the phasors for the three rays to form a triangle at both antennas, thus yielding relative SNR gain  $\eta = 0$ .

More generally, we can show that the combination of parameters for which  $\beta = 1$  (0 dB link margin) is too restrictive, and leads to an empty set for reflector distance  $r = 4 - 8$ m and transmission range  $R = 200$ m. This is because, when the combination of the two reflected rays falls into the danger zone for one of the receive antennas, it is possible to return to the danger zone after the additional phase rotations incurred by the two reflected rays in reaching the second antenna.

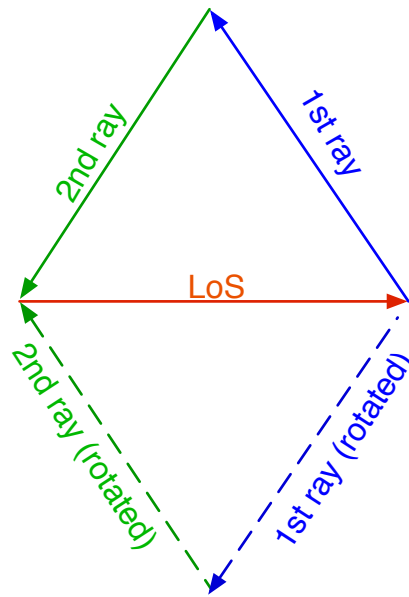


**Figure 3.4:** A complete fade at both antennas happen with a three-ray model for  $1 \times 2$  SIMO. For  $\alpha_1 = \alpha_2 = 1$ ,  $\gamma_1 = 2\pi/3$ , and  $\gamma_2 = 4\pi/3$ , we obtain  $|1 + e^{j(\pi-\phi_0)} + e^{j(\pi+\phi_0)}| = 0$  at the first receive antenna, and  $|1 + e^{j(\pi-\phi_0+2\pi/3)} + e^{j(\pi+\phi_0+4\pi/3)}| = 0$  at the second receive antenna.

To see this, we compute the relative SNR gain ( $\eta = |h_1|^2 + |h_2|^2$ ) as follows:

$$\begin{aligned} \eta &= 2 + 2\alpha_1^2 + 2\alpha_2^2 + 2\alpha_1\alpha_2 \cos(\phi_1 - \phi_2) + 2\alpha_1\alpha_2 \cos(\phi_1 - \phi_2 + \gamma_1 - \gamma_2) \\ &\quad - 2\alpha_1 \cos(\phi_1) - 2\alpha_2 \cos(\phi_2) - 2\alpha_1 \cos(\phi_1 + \gamma_1) - 2\alpha_1 \cos(\phi_2 + \gamma_2) \\ &\geq 2 - 4\alpha_1 \cos(\gamma_1/2) \cos(\phi_1 + \gamma_1/2) - 4\alpha_2 \cos(\gamma_2/2) \cos(\phi_2 + \gamma_2/2). \end{aligned} \quad (3.11)$$

Consider  $\beta = 1$  (link margin 0 dB). Choosing  $\gamma_i$  such that  $|4\alpha_i \cos(\gamma_i/2)| < 0.5$  ( $i = 1, 2$ ), we have  $|h_1|^2 + |h_2|^2 > 1$ . The corresponding antenna spacing falls in the range  $0.92 \cdot \max(\frac{R}{4r}) \ll \frac{d}{\lambda} \ll 1.08 \cdot \min(\frac{R}{4r})$ . However, this results in an *empty* set for reflector distance  $r = 4 - 8$  m and transmission range  $R = 200$  m.

While deterministic diversity is not possible, worst-case scenarios such as the one in Figure 3.4 are very unlikely under the statistical propagation model in Section 2.3.1, hence it is still possible to achieve *quasi-deterministic* diversity (e.g., an outage probability of  $10^{-4}$  at a link margin of 5 dB for  $1 \times 2$  SIMO), as we now demonstrate via simulations for the six-ray model. We briefly review the expressions for the SNR gain for the standard diversity schemes considered here (see [39, 41] for detailed discussion), followed by a discussion of design guidelines for antenna spacing.

### 3.3.2 MIMO SNR Gains

Given the propagation geometry and the antenna geometry, these can be computed using the simplified multi-ray channel model in Chapter 2.

**2 × 1 MISO Transmit Diversity:** The Alamouti scheme has  $\eta = (|h_1|^2 + |h_2|^2)/2$ , spatial matched filtering at the transmitter has  $\eta = |h_1|^2 + |h_2|^2$ , and selection diversity has  $\eta = \max(|h_1|^2, |h_2|^2)$ .

**1 × 2 SIMO Receive Diversity:** Maximal ratio combining (spatial matched filtering) has  $\eta = |h_1|^2 + |h_2|^2$ , and selection diversity has  $\eta = \max(|h_1|^2, |h_2|^2)$ .

In practice, one might prefer to use the preceding receive diversity schemes rather than the corresponding transmit diversity schemes, because of the feedback regarding channel state required by the latter.

**2 × 2 MIMO Diversity:** Denoting the channel matrix by  $H$ , we consider dominant eigenmode transmission, whose SNR gain  $\eta$  equals the largest eigenvalue of the Wishart matrix  $W = HH^H$ , and the Alamouti scheme, which has  $\eta = \frac{\text{trace}(W)}{2}$ .

In order to achieve robust performance, all of the schemes discussed above rely on the channel response between different antenna pairs being “different enough” that they are unlikely to encounter a destructive fade at the same time. We now discuss how to apply the analytical guidelines from Section 3.2 to ensure this.

### 3.3.3 Antenna Spacing

The outage probabilities for the various MIMO diversity schemes are plotted as a function of antenna spacing in Figure 3.5, keeping the link margin fixed at 5 dB. Some important observations are as follows.

- While we are unable to provide *deterministic* diversity for the six-ray model, design based on the analytical prescriptions from the two-ray model work very well for  $1 \times 2$  and  $2 \times 1$  systems, with antenna spacings of  $7 - 8\lambda$  providing the smallest outage probabilities.
- Smaller spacing can be used for  $2 \times 2$  MIMO diversity, but the spacing designed for  $1 \times 2$  SIMO still works well. In particular, a larger range of antenna spacing ( $3 - 10\lambda$ ) works well for the  $2 \times 2$  MIMO system.
- Performance as a function of antenna spacing has a quasi-periodic structure, with the SIMO/MISO schemes showing another local optimum in performance around  $23\lambda$ . The difference from the first optimum ( $7 - 8\lambda$ ) is about  $15 - 16\lambda$ . From our analysis (in Section 3.2), we know that the periodicity in  $\frac{d}{\lambda}$  for a single reflector at distance  $r$  is exactly  $\frac{R}{2r}$ . For  $R = 200$  m, quasi-periodicity of  $15 - 16\lambda$  corresponds to an effective range of about  $r_{eff} = 6.25-6.67$  m, which is approximately the midpoint of the range of about 4-10 m which creates strong reflected rays for the antenna patterns of interest. Of course, this is of little relevance to

design, since we would rather operate at smaller antenna spacings of  $d = 7 - 8\lambda$ : the performance is significantly better and the form factor is more compact than at the next local optimum of  $d = 23\lambda$ .

- When the antenna spacing is too large, then the phases seen by the different antennas get randomized, in which the performance is closer to that in a probabilistic i.i.d. Rayleigh fading style regime, for which dual diversity with a small link margin does not give good performance. For selective receive diversity, the outage probability for i.i.d. Rayleigh fading is given by  $(1 - \exp(-\beta/\overline{|h|^2}))^2$ , where  $\overline{|h|^2}$  denotes the mean power (greater than the LoS benchmark of one because of the contribution of reflected rays). From ray tracing simulations, the mean power is obtained as  $\overline{|h|^2} = 1.31$ , which leads to a predicted outage probability of 4.44% for a link margin of 5 dB, and matches closely with the outage probability of 4.8% obtained by direct simulations using ray tracing. In contrast, the outage rates at a spacing of  $7 - 8\lambda$  are less than  $10^{-4}$ , or two orders of magnitude better. Thus, when antenna spacings are carefully chosen for sparse multipath channels, we can obtain far better performance than for i.i.d. Rayleigh fading.

We now provide additional numerical results illustrating quasi-deterministic diversity. Figure 3.6(a) plots the outage probability as a function of the link margin for a  $1 \times 2$  SIMO link. We see that  $d = 8\lambda$  gives the best outage probability for both the selective diversity scheme and maximal ratio combining scheme in

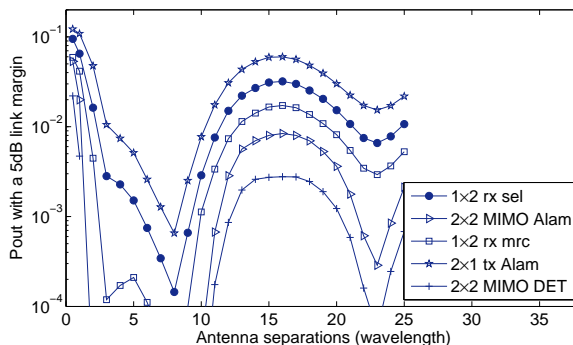
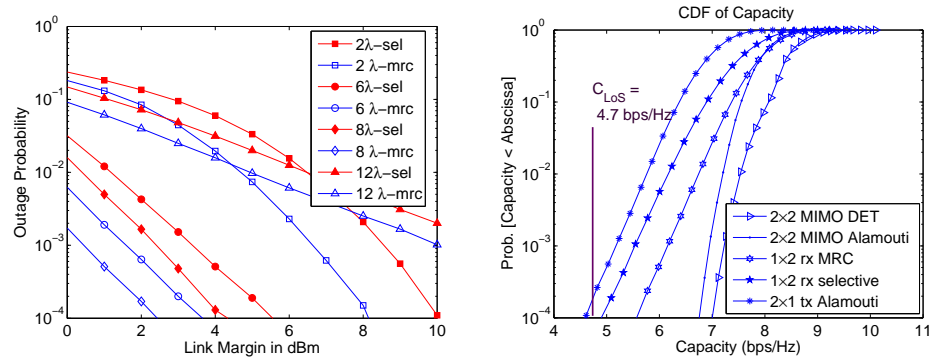


**Figure 3.5:** Outage probabilities versus antenna spacing for different diversity strategies (5 dB link margin).

the  $1 \times 2$  SIMO system (better than  $10^{-4}$  at link margins of 4.4 dB and 2.4 dB, respectively), but that the performance starts deteriorating when the spacing is too low ( $d = 2\lambda$ ) or too high ( $d = 12\lambda$ ). Figure 3.6(b) plots the CDF of the channel capacity for a variety of diversity strategies, fixing antenna spacing at  $8\lambda$  and link margin at 5 dB. The capacity is given by  $C = \log_2(1 + \eta SNR_{LoS})$ , where  $\eta$  denotes the SNR gain (for a given diversity strategy) and  $SNR_{LoS}$  represents the nominal received SNR for the SISO LoS benchmark. For reference, the capacity of an idealized LoS SISO system, denoted as  $C_{LoS}$ , equals 4.7 bps/Hz. At an outage probability of  $10^{-4}$ , the diversity strategies in the  $2 \times 2$  MIMO system and the  $1 \times 2$  SIMO system achieve outage capacity higher than  $C_{LoS}$ , while the  $2 \times 1$  MISO transmit Alamouti diversity has a slightly smaller outage capacity of 4.6 bps/Hz.



(a) Outage probability versus link margin for different antenna spacings ( $2\lambda$ ,  $6\lambda$ ,  $8\lambda$ ,  $12\lambda$ ) using the selective diversity (sel) and maximal ratio combining (mrc). (b) CDF of channel capacity for different antenna spacings ( $2\lambda$ ,  $6\lambda$ ,  $8\lambda$ ,  $12\lambda$ ) using the selective diversity (sel) and maximal ratio combining (mrc).

**Figure 3.6:** Simulation results for spatial diversity.

## Chapter 4

# Frequency Diversity for Wideband Channel

The communication bandwidths for the 60 GHz unlicensed band, as well as for other mm wave systems, are expected to be of the order of GHz, and can therefore potentially provide significant frequency diversity. In this chapter, we focus on providing analytical insight into when deterministic frequency diversity is possible. More extensive numerical results are postponed to the next chapter, when we discuss combined spatial and frequency diversity.

For the simplified multi-ray channel model (2.7), define the relative channel frequency response as follows:

$$H(f) = 1 + \sum_{i=1}^{N_r-1} \alpha_i e^{-j(\phi_i + 2\pi f\tau_i)}, \quad -B/2 \leq f \leq B/2, \quad (4.1)$$

where  $B$  is the channel bandwidth.

**Frequency diversity gain:** A convenient performance measure for characterizing the effect of frequency diversity is the channel power gain averaged over the available bandwidth  $B$ . We term this the *frequency diversity gain*, and define it as:

$$G(B) = \frac{1}{B} \int_{-B/2}^{B/2} |H(f)|^2 df \quad (4.2)$$

This provides a measure of the average SNR gain (averaged over the band) relative to our reference SISO LoS link.

**Upper bound on Shannon capacity:** The Shannon limit for channel spectral efficiency is given by averaging over the band as follows:

$$C_s = \frac{1}{B} \int_{-B/2}^{B/2} \log(1 + SNR_{LoS} |H(f)|^2) df$$

By the concavity of the logarithm, taking the average inside the log gives an upper bound, using Jensen's inequality, we therefore obtain that

$$C_s \leq \log(1 + SNR_{LoS} G(B))$$

Thus, the frequency diversity gain provides an upper bound on the Shannon capacity. For low SNR, the upper bound is expected to be tight, since  $\log(1+x) \approx x$  for small  $x$ . However, our simulations show that the upper bound provides an excellent approximation even for moderate SNRs in the range 10-20 dB. We therefore focus on characterizing the behavior of the frequency diversity gain  $G(B)$ , which

is far more analytically tractable than the Shannon capacity, for providing analytical design insights. We then employ simulation results to verify that the resulting design prescriptions provide robust performance in terms of Shannon capacity as well. These show that the discrepancy in spectral efficiency is less than 0.2 bps/Hz, corresponding to about 0.2 dB for the SNR ranges of interest.

We obtain analytical insight for a three-ray model which, as discussed before, captures the strongest components of a typical lamppost-based link (LoS, near wall reflection and street reflection). The frequency diversity gain is given by

$$G(B) = 1 + \alpha_1^2 + \alpha_2^2 + 2\alpha_1 \text{sinc}(B\tau_1) \cos \phi_1 + 2\alpha_2 \text{sinc}(B\tau_2) \cos \phi_2 \quad (4.3)$$

$$+ 2\alpha_1\alpha_2 \text{sinc}(B(\tau_1 - \tau_2)) \cos(\phi_1 - \phi_2)$$

**Deterministic frequency diversity:** From (4.3), we observe that  $G(B)$  depends on the bandwidth-delay products  $B\tau_i$ , given the amplitudes and phases of the reflected paths  $\alpha_i$  and  $\phi_i$  ( $i = 1, 2$ ). Since

$$\alpha_1^2 + \alpha_2^2 + 2\alpha_1\alpha_2 \text{sinc}(B(\tau_1 - \tau_2)) \cos(\phi_1 - \phi_2) \geq \alpha_1^2 + \alpha_2^2 - 2\alpha_1\alpha_2 = (\alpha_1 - \alpha_2)^2 \geq 0 \quad (4.4)$$

we can lower bound the frequency diversity gain as

$$G(B) \geq \max(1 + 2\alpha_1 \text{sinc}(B\tau_1) \cos \phi_1 + 2\alpha_2 \text{sinc}(B\tau_2) \cos \phi_2, 0) \quad (4.5)$$

We can now show that it is possible to provide deterministic performance guarantees when  $B \geq \frac{1}{\tau_{min}}$ , where  $\tau_{min} = \min\{\tau_1, \tau_2\}$ . To see this, note that  $\min_{x \geq 1} \text{sinc}(x) =$

$\text{sinc}(1.5) = -\frac{2}{3\pi}$ . Plugging this into (4.5), we find the following lower bound (setting  $\alpha_1 = \alpha_2 = 1$ , and  $\phi_1$  and  $\phi_2$  to odd multiples of  $\pi$ )

$$G(B) \geq 1 - \frac{8}{3\pi} \approx 0.15 \quad (4.6)$$

which corresponds to a link margin of 8.2 dB. However, this is far too pessimistic an estimate. The lower bound in (4.4) is realized when  $\phi_1 - \phi_2$  is an odd multiple of  $\pi$ , whereas the further bounding of (4.5) to obtain (4.6) requires that both  $\phi_1$  and  $\phi_2$  are odd multiples of  $\pi$  (in which case their difference is an even multiple of  $\pi$ ), so that the overall lower bound (4.6) is loose. Doing a brute force numerical minimization of (4.3) over  $\alpha_i \in [0, 1]$ ,  $\phi_i \in [0, 2\pi]$ , and  $B\tau_i \geq 1$ , we obtain that  $G(B) \geq 0.81$ , corresponding to a link margin of less than 1 dB for deterministic diversity.

When  $B\tau_{min} < 1$ , then we can no longer provide deterministic guarantees with frequency diversity alone, and spatial diversity becomes essential for providing robust performance, as discussed in the next chapter.

## Chapter 5

# Combined Frequency and Spatial Diversity

We noted in the previous chapter that frequency diversity alone is not sufficient to provide a robust link when the bandwidth is smaller than the inverse of the minimum delay spread. We now show that combining frequency diversity with spatial diversity can provide robust performance over a broad set of scenarios. Specifically, consider a  $1 \times 2$  SIMO link, with receive antennas spaced by  $8\lambda$  (following the design prescriptions from Section 3.3.3) using MRC at each frequency (as one might do in an OFDM system). The combined frequency diversity gain can now be defined as

$$G^{(2)}(B) = \frac{1}{B} \int_{-B/2}^{B/2} (|H_1(f)|^2 + |H_2(f)|^2) df = G_1(B) + G_2(B) \quad (5.1)$$

where the gain due to antenna 1 is given by  $G_1(B) = G(B)$  as in (4.3), while the gain due to the second antenna is given by

$$G_2(B) = 1 + 2\alpha_1 \text{sinc}(B\tau_1) \cos(\phi_1 + \gamma_1) + 2\alpha_2 \text{sinc}(B\tau_2) \cos(\phi_2 + \gamma_2) \quad (5.2)$$

$$+ \alpha_1^2 + \alpha_2^2 + 2\alpha_1\alpha_2 \text{sinc}(B(\tau_1 - \tau_2)) \cos(\phi_1 - \phi_2 + \gamma_1 - \gamma_2).$$

## 5.1 Outage Probability

Outage probabilities are defined in terms of the frequency diversity gains as  $P_{out} = P[G(B) < \beta^2]$  for SISO and  $P_{out} = P[G^{(2)}(B) < \beta^2]$  for SIMO, and are plotted in Figure 5.1. For our propagation model in Section 2.3.1, the deterministic frequency diversity criterion  $B\tau_{min} \geq 1$  is satisfied for a bandwidth of 2 GHz, since the minimum delay difference is about 0.5 ns ( $r_{wall} = 4$  m and  $R = 200$  m). We now make the following observations:

1. For a given link margin, the outage probability decreases as the channel bandwidth increases from 100 MHz to 2 GHz in both the SISO and the  $1 \times 2$  SIMO systems.
2. An outage probability of  $10^{-4}$  is achieved with the 2 GHz bandwidth for  $\beta^2 = 0.9$  and  $\beta^2 = 1.9$  for SISO and SIMO, respectively, corresponding to link margins of 0.45 dB and -2.8 dB relative to LoS SISO. The negative link

margin of -2.8 dB represents a gain over SISO LoS which is almost as high as the 3 dB gain that would be expected from ideal MRC over an AWGN channel.

3. When  $B < 1/\tau_{min}$ , frequency diversity alone does not suffice. For bandwidths of 100 MHz and 250 MHz,  $\beta^2 = 0.08$  and  $\beta^2 = 0.14$  (corresponding link margins of 11 dB and 8.53 dB) are obtained at  $10^{-4}$  outage probability. However, combined frequency and spatial diversity provide  $\beta^2 = 0.41$  and  $\beta^2 = 0.82$  (corresponds to link margins of 3.8 dB and 0.86 dB) at  $10^{-4}$  outage probability. Thus, quasi-deterministic diversity can be obtained even when  $B < 1/\tau_{min}$  in a SIMO link.
4. For both SISO and  $1 \times 2$  SIMO, increasing bandwidth from 2 GHz to 3 GHz does not further decrease the outage probability. Thus,  $B = 1/\tau_{min}$  suffices in terms of providing frequency diversity.

While the three-ray channel model is used in these simulations, we note that the more complete six-ray actually gives slightly better performance, possibly due to the additional averaging provided by the additional paths.

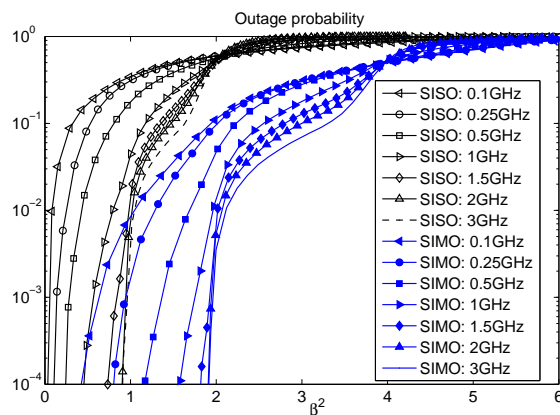


**Figure 5.1:** Outage probabilities for SISO and  $1 \times 2$  SIMO links as a function of channel bandwidth.

## 5.2 Robustness to Changes in Propagation Environment

The preceding discussions show that it is possible to provide quasi-deterministic guarantees by choosing antenna spacing and bandwidth as a function of the nominal geometry. Suppose, for example, that we have designed a SIMO link with antenna spacing of  $8\lambda$  and bandwidth 2 GHz, thus providing quasi-deterministic guarantees for our nominal geometry. We now provide two examples showing the robustness of this design to variations in the propagation environment.

**Reduction in minimum delay:** While  $B > \frac{1}{\tau_{min}}$  for our nominal environment, a truck of height 3.4m parked halfway between the transmitter and receiver reduces the range of  $r_{street}$  from [4m, 8m] to [0.6 m, 4.6 m], yielding  $\tau_{min} = 0.012\text{ns}$  (the

distance for the near wall reflector remains in the same range as before). The link bandwidth of 2 GHz is now much smaller than  $1/\tau_{min} = 83$  GHz. Table 5.1 shows the link margins required for an outage probability of  $10^{-4}$  for various bandwidths in this scenario, for both SISO and SIMO links. The table shows that it is still possible to provide quasi-deterministic diversity: for 2 GHz bandwidth, the link margins for  $10^{-4}$  outage are 4.8 dB for SISO and 1.45 dB for SIMO.

**Table 5.1:** Required link margins (LM) to achieve  $10^{-4}$  outage probability.

| BW (GHz)        | 0.1 | 0.25 | 0.5 | 1   | 1.5  | 2    | 3    |
|-----------------|-----|------|-----|-----|------|------|------|
| LM in SISO (dB) | 17  | 12.2 | 8   | 5.4 | 4.9  | 4.8  | 4.7  |
| LM in SIMO (dB) | 8.5 | 4.7  | 2.1 | 1.5 | 1.48 | 1.45 | 1.42 |

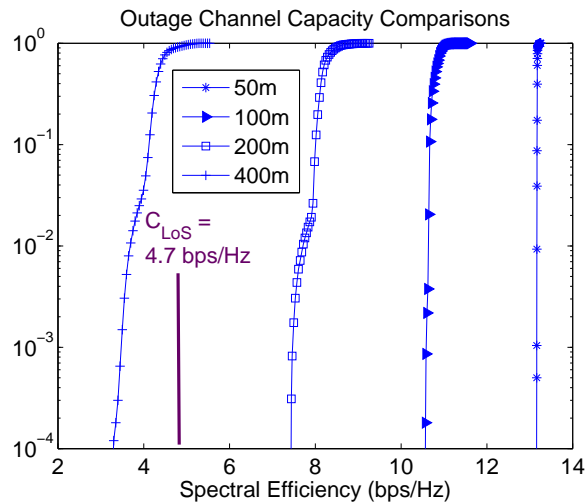


**Figure 5.2:** Probability of outage as a function of link range.

**Change in link range:** We now plot, in Figure 5.2, outage probabilities for our nominal design (2 GHz bandwidth,  $8\lambda$  spacing) for 200 m link range for several

link ranges: 50 m, 100 m, 200 m and 400 m. We use the same horn antenna with the directivity gain of 21.3 dBi and set the transmit power to be 18.7 dBm in order to fully utilize the FCC limit of 40 dBm average EIRP. Assuming a loss of 4 dB due to heavy rain (56.4 mm/hour), this yields  $SNR_{LoS}$  of 19.2 dB at the nominal link range of 200 m. We add a 5.2 dB margin to set the benchmark  $SNR_{LoS}$  at 14 dB, corresponding to uncoded BER of  $10^{-9}$  with QPSK, and a Shannon limit of 4.7 bps/Hz. The outage capacity at  $10^{-4}$  outage probability is higher than this benchmark spectral efficiency for link ranges of 50 m, 100 m and 200 m. For 400 m, an outage capacity of 3.3 bps/Hz is achieved at  $10^{-4}$  outage probability. This is 1.4 bps/Hz smaller than the reference Shannon limit at 200 m because of 13.2 dB additional attenuation (6 dB due to free space propagation, 3.2 dB due to oxygen absorption, and 4 dB due to rain attenuation). In addition, the outage probability curve is less steep at 400m because of more severe fading (the reflected rays are comparable in strength to the LoS path due to the small grazing angle). The opposite effect (steeper curve) is seen at smaller link ranges due to weaker reflections.

**Change in Reflection Surfaces:** We now provide example simulation results that show that our qualitative conclusions hold under variants of the model for the reflection coefficients. We compare results for smooth reflection surfaces with thick specimen (Fresnel reflection surfaces) with results for rough surfaces with

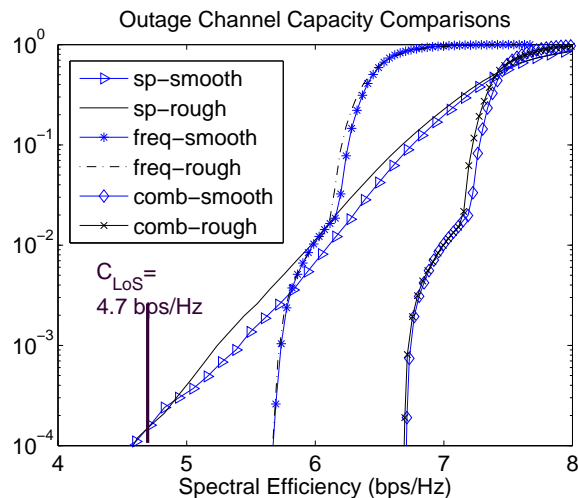


**Figure 5.3:** Outage capacity for different reflection surfaces for spatial diversity, frequency diversity and combined diversity.

thin specimen (multilayer model with multiplicative scattering loss), using the six-ray channel model for our nominal design (2 GHz bandwidth,  $8\lambda$  antenna spacing). For our nominal design (2 GHz bandwidth,  $8\lambda$  antenna spacing), we use the six-ray model to estimate the CDF of channel capacity, as plotted in Figure 5.3 for the following scenarios: 1)  $1 \times 2$  narrowband SIMO (spatial diversity alone), 2) wideband SISO (frequency diversity alone), 3)  $1 \times 2$  wideband SIMO with MRC (combined diversity). A 3 dB link margin is employed relative to the LoS SISO benchmark, setting  $SNR_{LoS} = 14$  dB. For smooth reflection (as in the rest of the thesis), we consider wood for wall reflection and concrete for ground reflection. For rough reflection, the ground reflection is from aerated concrete [38] with dielectric constant  $\epsilon_c = 2.25 - 0.1j$ , thickness  $d_{thk} = 5cm$  and

surface standard deviation  $\sigma_h = 0.2mm$ , and the wall reflections are from rough glasses [38] with  $\epsilon_c = 8.9 - 0.13j$ ,  $d_{thk} = 0.4cm$  and  $\sigma_h = 0.3mm$ . All schemes provide high spectral efficiencies with quasi-deterministic reliability ( $10^{-4}$  outage probability): compared to  $C_{LoS} = 4.7$  bps/Hz, SISO with frequency diversity is 1 bps/Hz higher, SIMO with combined diversity is 2 bps/Hz higher, while narrowband SIMO is 0.2 bps/Hz lower. Therefore, we conclude that the outage capacities for smooth and rough surfaces are barely distinguishable (less than 0.2 bps/Hz), and that all schemes provide quasi-deterministic performance.

# Chapter 6

## Analog Multitone

In this chapter, we investigate the use of analog multitone for sidestepping the ADC bottleneck for multiGigabit communications: transmissions are split into a number of subbands, each of which can be separately sampled at the receiver using a lower rate ADC. In order to combat the severe fading and inter carrier interference, we investigate four different linear equalization strategies and show that it is essential to perform equalization for the samples from both arrays to achieve the robust transmissions.

### 6.1 Introduction

For frequency selective wideband channels, standard DSP-based approaches to channel dispersion using time-domain equalization or OFDM both require high-speed ADCs with large dynamic range and high precision: OFDM has an inher-

ently large Peak-to-Average Power Ratio (PAPR), while multipath propagation creates large dynamic range even for singlecarrier transmission. High speed, high-precision ADCs based on conventional architectures, such as flash ADCs, are too costly or power-hungry [28]. Time-interleaved ADCs [29] have been proposed as a solution: a high rate ADC is synthesized using a number of slower ADCs whose sampling times are staggered, thereby providing a power efficient option. However, even though the sub-ADCs operate at a lower rate, the sample-and-hold blocks in each of the sub-ADCs still need to operate over the entire signal bandwidth, leading to issues of bandwidth scalability. In this chapter, we investigate Analog Multitone (AMT) as a solution to the ADC bottleneck: the idea is to transmit in parallel over a small number of subbands (significantly smaller than the number of subcarriers employed by OFDM), each of which can be sampled using a relatively low rate ADC after analog filtering at the receiver. There are two advantages in splitting the transmissions into a number of subbands (say  $M$ ). First, since each subband is smaller by a factor of  $M$  and transmissions happen in parallel over different subbands, it suffices to sample each subband with an ADC that is  $M$  times slower (including the sample-and-hold block). Second, the equivalent channel seen by the symbols over small subbands is significantly shorter than the channel seen over the entire band. For example, we see from the top panel of Figure 6.1 that the channel over the entire band has 24 taps. However, when we

split the entire band into 4 or 8 subbands, the channel in one of the subbands has only 8 and 6 taps respectively. As a result, the equalization complexity in each subband is reduced substantially, and simple equalizers can be implemented in parallel.

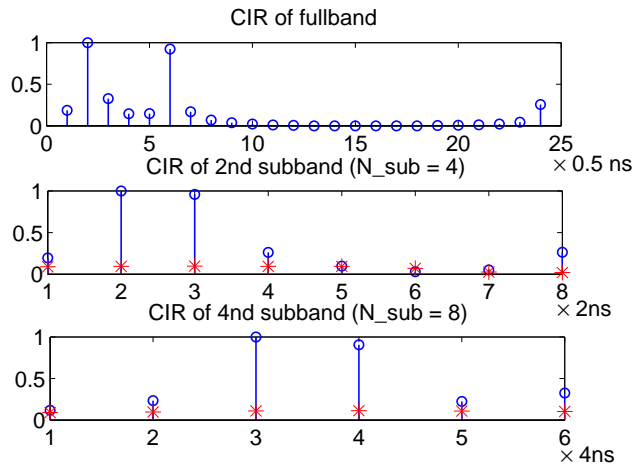


**Figure 6.1:** Illustration of normalized channel impulse responses of a system of 2 GHz bandwidth at 60 GHz band with different number of subbands (The star marker denotes the ICI signal from the adjacent subband on the left).

The AMT scheme considered here employs excess bandwidth in each subband in order to limit peak amplitude and ISI, but does not provide guard bands between adjacent subbands, in order to avoid spectral wastage. This implies that we must combat ICI across subbands, in addition to the ISI within a subband due to channel dispersion. While AMT is a generic technique for decomposing high-rate channels into slower subchannels, we also need to combine it with features specific

to 60 GHz. In particular, directional transmission and reception are critical to attaining the link budget at 60 GHz, and can be attained using compact printed circuit antenna arrays; we therefore consider beamforming with  $4 \times 4$  antenna arrays in our modeling and performance evaluation. In Chapter 5, we have shown that a combined diversity scheme that employs both frequency and spatial diversity can yield extremely robust performance relative to the LoS link. In the following work, we propose and evaluate different equalizer schemes for realizing these performance advantages, using Analog Multitone with one transmit antenna array and two receive antenna arrays separated by a few wavelengths.

**Contributions:** We propose an Analog Multitone scheme for communication over dispersive channels spanning 2 GHz of bandwidth in the millimeter wave band. We consider a system with a  $4 \times 4$  transmit array, and two  $4 \times 4$  receive arrays. The arrays at the transmitter and receiver beamform towards each other along the Line-of-Sight (LoS) path (for simplicity, we do not consider spatial multipath combining or suppression). We derive an equivalent channel between the transmitter and the receivers that accounts for the beamforming patterns and the physical multipath channel, consisting of reflections off a nearby wall and the ground in addition to the LoS path. We split the transmissions into four or eight subbands and investigate four linear equalization strategies for demodulating each subband. These strategies are based on different combinations of the following

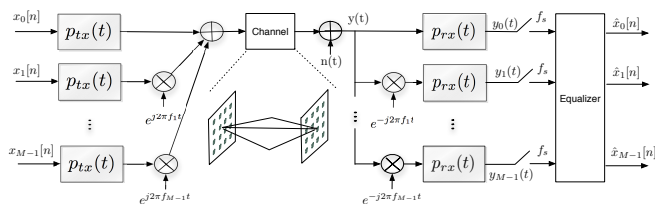


**Figure 6.2:** Block diagram of the analog multitone system (only one of the two receive arrays is shown for simplicity).

choices: (a) Combine samples from both arrays optimally or choose samples from the array that sees the stronger channel in the subband and (b) Treat the interference from adjacent subbands as noise or exploit the structure of the interference from adjacent subbands. While we consider two receive arrays in order to provide spatial diversity, we find that the additional degrees of freedom provided by combining samples from both arrays provide much better interference suppression (avoiding error floors) than using only samples from the array which sees a stronger channel.

**Related work:** The concept of analog multitone was proposed nearly four decades ago, but was rendered obsolete by the emergence of OFDM. However, it was revived recently for supporting high data rates (10 – 20 Gbps) over backplane links [42] [43]. These systems allocate substantial guard bands between the different subbands, thereby simplifying the equalizer, but reducing the spectral efficiency. In contrast, we let the subbands overlap and account for ICI as well as ISI, and include features (such as beamforming and spatial diversity) specific to the

wireless application at hand. A channelized digital receiver for ultra wide band (UWB) signals was proposed in [44]. The receiver employs several low-rate ADCs, each sampling in a small subband, but the transmission is over the entire band, hence received samples from different subbands need to be pooled for equalization, unlike our system, where equalization for each subband can be performed in parallel. The idea of splitting the transmission into subbands with zero guard band has been investigated before in cosine modulated multitone (CMT) systems [45], but this system, which is designed for flat fading (rather than frequency selective fading as considered here) discards half the available degrees of freedom in order to avoid ICI.

## 6.2 System Model

We provide an example link budget, and then derive an equivalent channel model (for a typical 60 GHz multipath channel) for fixed transmit and receive beamforming weights. This is then used to set up a complex baseband model for the AMT scheme.

### 6.2.1 Link Budget and Channel Model

**Link Budget:** We consider transmission and reception using  $4 \times 4$  arrays, where each element in the array is a microstrip antenna with a directivity gain of 7 dBi and the spacing between adjacent elements is  $\lambda/2 = 2.5\text{mm}$ . Since a  $4 \times 4$  array provides a 12 dBi beamforming gain, the maximum allowable transmit power is 21 dBm (after accounting for the directivity gain of 7 dBi) to fully utilize the FCC limit of 40 dBm average EIRP [32]. This requires only 9dBm power output from each of the 16 power amplifiers, and is sufficient to support high data rate links across distances of 200m: for example, we can transmit data at 4 Gbps using QPSK modulation over a bandwidth of 2GHz, after budgeting for an oxygen absorption loss of 16dB/km, a link margin of 5dB and a noise figure of 5dB.

**Beamforming Weights:** We consider transmission from one  $4 \times 4$  array to a receiver with two such arrays, with the receive arrays being separated by a few wavelengths. The arrays are mounted on top of lampposts and the transmit and receive arrays are separated by 100s of meters. We choose the transmit and receive phases as in [46]: (a) the phases at the receive antennas are chosen so that each array beamforms to the center of the transmit array and (b) the phases at the transmit elements are chosen so that the transmitter beamforms to the midpoint of the line joining the centers of the two receive arrays.

**Equivalent channel model:** The channel between the transmit and receive arrays consists of reflections from the ground and a nearby wall in addition to the LoS path. Suppose that there are  $L$  reflected paths and an LoS path (which we index to be the 0th path). The channel is then given by

$$h(t) = \sum_{l=0}^L g_{prop}[l] g_{BF}^{tx}[l] g_{BF}^{rx}[l] \delta(t - t_l), \quad (6.1)$$

where  $g_{prop}[l]$ ,  $g_{BF}^{tx}[l]$ ,  $g_{BF}^{rx}[l]$  and  $t_l$  denote the propagation loss, beamforming gain at the transmitter, beamforming gain at the receiver and the propagation delay along the  $l$ th path respectively. We now specify each of these terms explicitly.

The propagation term along the LoS path is given by

$$g_{prop}[0] = \frac{\lambda}{4\pi R_0} e^{-\frac{K_p R_0}{2}} e^{-j\frac{2\pi R_0}{\lambda}}, \quad (6.2)$$

where  $R_0$  is the distance along the LoS path and  $K_p = 0.0016 \ln 10$  is the oxygen absorption (16 dB/km) at 60 GHz. The propagation term along the  $l$ th reflected path is similar (substituting  $R_l$  for  $R_0$ ), except that also we need to include a multiplicative factor  $A_l$  to account for the reflection coefficient.

Consider the beamforming gain  $g_{BF}^{tx}[0]$  at the transmitter along the LoS path. Assuming that this path makes angles  $(\theta_{t0}, \phi_{t0})$  with the normal of the transmit array and one of the sides of the array respectively, the beamforming gain at the

transmitter is given by

$$g_{BF}^{tx}[0] = \sqrt{\rho_{t0}N_t}, \quad (6.3)$$

where  $\rho_{t0}$  is the directivity gain of an antenna element along  $(\theta_{t0}, \phi_{t0})$  and  $N_t$  is the number of elements in the transmit array. Analogously, the beamforming gain at the receiver  $g_{BF}^{rx}[0] = \sqrt{\rho_{r0}N_r}$ , where  $\rho_{r0}$  is the directivity gain of an antenna element along the receive direction  $(\theta_{r0}, \phi_{r0})$  and  $N_r$  is the number of receive antenna elements.

Next, we specify the beamforming gains at the transmitter along the  $l$ th path. Let us denote the propagation delay from the  $i$ th transmit element to the center of the receive array along the  $l$ th path by  $d_{il}$ . Then, the beamforming gain at the transmitter along this path is given by

$$g_{BF}^{tx}[l] = \sqrt{\frac{\rho_{tl}}{N_t}} \sum_{i=1}^{N_t} e^{-j(2\pi f_c(d_{il}-d)+\beta_i)}, \quad (6.4)$$

where  $\rho_{tl}$  is the directivity gain along the  $l$ th path  $(\theta_{tl}, \phi_{tl})$ ,  $d$  is the propagation delay from the reference element to the center of the receive array and  $\{\beta_i\}$  are the beamforming weights. The beamforming gain at the receiver  $g_{BF}^{rx}[l]$  can be computed analogously.

For concreteness, we also specify the antenna patterns to compute the directivity gains along different paths. The normalized microstrip antenna element

gain along the direction  $(\theta, \phi)$  is given by [31]:

$$\rho(\theta, \phi) = (\cos^2 \theta \sin^2 \phi + \cos^2 \phi) \left| \cos(\pi v_x) \frac{\sin(\pi v_y)}{\pi v_y} \right|^2, \quad (6.5)$$

where  $v_x = L \sin \theta / \lambda$  and  $v_y = W \sin \theta / \lambda$ , with  $L$  and  $W$  being the length and width of the microstrip antenna patch respectively. We choose  $L = W = 0.5\lambda / \sqrt{\epsilon_r}$ , with the relative permittivity of the dielectric substrate  $\epsilon_r = 2.17$  ([47]).

### 6.2.2 Complex Baseband Model

Figure 6.2 shows a complex baseband model of the system. We split the transmission into  $M$  subbands. The symbols in the  $m$ th subband  $\{x_m[n]\}$  pass through a transmit filter  $p_{tx}(t)$  (square-root raised cosine) and are then upconverted to a frequency  $f_m = f_c + m\Delta f, m = 0, 1, \dots, M - 1$  where  $\Delta f$  is the spacing between adjacent subbands. To achieve high bandwidth efficiencies, we allow the different subcarrier bands to overlap as shown in Figure 6.3. At the receiver, we recover the symbols from the  $m$ th subband by downconverting it to baseband, passing it through a receive filter  $p_{rx}(t)$  (also square-root raised cosine) and sampling each subband at its Nyquist rate. We then pass these samples through an equalizer to eliminate the intercarrier interference before we estimate the symbols.

Denoting the channel seen by one of the receive arrays by  $h(t)$ , we derive an expression for the samples received from this array. The received signal before

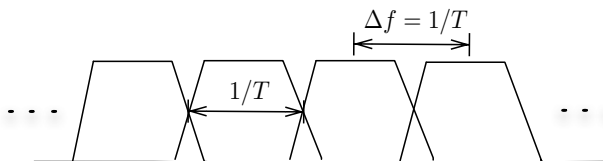


**Figure 6.3:** Illustration of the subband allocation.

subband separation  $y(t)$  is given by

$$y(t) = \sum_{m=0}^{M-1} \left( \sum_n x_m[n] p_{tx}(t - nT) e^{j2\pi f_m t} \right) \otimes h(t) + n(t) \quad (6.6)$$

where  $\otimes$  denotes convolution,  $T$  is the symbol period and  $n(t)$  is additive white Gaussian noise with two-sided power spectral density of  $N_0/2$ . The signal in the  $m$ th subband after the receive filter  $y_m(t)$  consists of the following parts: the desired transmitted signal from the  $m$ th subband (denoted by  $y_{m \rightarrow m}(t)$ ) and the intercarrier interference signal from the  $m - 1^{th}$  and  $m + 1^{th}$  subbands (denoted by  $y_{m-1 \rightarrow m}(t)$  and  $y_{m+1 \rightarrow m}(t)$  respectively). Thus, we have:

$$y_m(t) = y_{m \rightarrow m}(t) + y_{m-1 \rightarrow m}(t) + y_{m+1 \rightarrow m}(t) + n_m(t), \quad (6.7)$$

where the noise term  $n_m(t) = (n(t) e^{-j2\pi f_m t}) \otimes p_{rx}(t)$ . Denoting the channel taps by  $h(t) = \sum_{l=0}^L \alpha_l \delta(t - t_l)$ , we can get explicit expressions for the contributions from different subbands as follows:

$$y_{m \rightarrow m}(t) = \sum_n x_m[n] \otimes h_{m \rightarrow m}(t) = \sum_n \sum_{l=0}^L \alpha_l x_m[n] e^{-j2\pi f_m t_l} (p_{tx} \otimes p_{rx})(t - nT - t_l), \quad (6.8)$$

$$y_{m-1 \rightarrow m}(t) = \sum_n x_m[n] \otimes h_{m-1 \rightarrow m}(t) = \sum_n \sum_{l=0}^L \alpha_l x_{m-1}[n] e^{-j2\pi f_m \tau_l} e^{-j2\pi \Delta f n T} (p_{tx}^- \otimes p_{rx}) (t - nT - t_l), \quad (6.9)$$

$$y_{m+1 \rightarrow m}(t) = \sum_n x_m[n] \otimes h_{m+1 \rightarrow m}(t) = \sum_n \sum_{l=0}^L \alpha_l x_{m+1}[n] e^{-j2\pi f_m \tau_l} e^{j2\pi \Delta f n T} (p_{tx}^+ \otimes p_{rx}) (t - nT - t_l), \quad (6.10)$$

with  $p_{tx}^-(t) = p_{tx}(t)e^{-j2\pi \Delta f t}$  and  $p_{tx}^+(t) = p_{tx}(t)e^{j2\pi \Delta f t}$ . From these equations, we see that the symbols see a time invariant channel if we choose  $T\Delta f = 1$ .

We define  $h_m(t) = \sum_{l=1}^L \alpha_l e^{-j2\pi f_m \tau_l} \delta(t - \tau_l)$ . By sampling  $y_m(t)$  at a frequency  $1/T$ , we obtain the discrete sequence  $y_m[k]$ :

$$y_m[k] = \sum_n (x_m[n] p_m(kT - nT) + x_{m-1}[n] p_m^-(kT - nT) + x_{m+1}[n] p_m^+(kT - nT)) + n_m[k], \quad (6.11)$$

where  $p_m(t) = p_{tx} \otimes h_m \otimes p_{rx}(t)$  and  $p_m^-(t) = p_{tx}^- \otimes h_m \otimes p_{rx}(t)$  and  $p_m^+(t) = p_{tx}^+ \otimes h_m \otimes p_{rx}(t)$ . The discrete channel seen by the symbol  $x_m[n]$  is given by  $(p_m[0], p_m[1], \dots)$ , where  $p_m[i] = p_m(iT)$ . The channels seen by the symbols from the  $m-1^{th}$  and  $m+1^{th}$  bands are defined analogously, with  $p_m^-$  and  $p_m^+$  taking the place of  $p_m$ .

We truncate the channel response at a point where its samples are 40dB below the largest sample and denote the resulting length by  $v$ . In matrix-vector notation,

the received samples in the  $m$ th subband, denoted by  $\mathbf{y}_m[n]$ , are given by

$$\begin{aligned} \mathbf{y}_m[n] &= \mathbf{H}_{m,m}\mathbf{x}_m[n] + \mathbf{H}_{m,m-1}\mathbf{x}_{m-1}[n] \\ &+ \mathbf{H}_{m,m+1}\mathbf{x}_{m+1}[n] + \mathbf{n}_m[n], \end{aligned} \quad (6.12)$$

where

$$\mathbf{H}_{m,m} = \begin{bmatrix} p_m[0] & \cdots & p_m[v] & 0 & 0 & 0 \\ 0 & p_m[0] & \cdots & p_m[v] & 0 & 0 \\ 0 & 0 & \cdots & \cdots & \cdots & 0 \\ 0 & 0 & 0 & p_m[0] & \cdots & p_m[v] \end{bmatrix}^T,$$

$$\mathbf{x}_m[n] = [\cdots x_m[n-1], x_m[n], x_m[n+1], \cdots]^T,$$

$$\mathbf{n}_m[n] = [\cdots n_m[n-1], n_m[n], n_m[n+1], \cdots]^T,$$

and  $\mathbf{H}_{m,m-1}, \mathbf{H}_{m,m+1}$  are defined in a manner similar to  $\mathbf{H}_{m,m}$  with  $p_m^-$  and  $p_m^+$  in place of  $p_m$  respectively.

The samples from the  $m$ th subband of the other receive array satisfy a similar model with a different set of channel matrices.

### 6.3 Equalization Schemes

In this section, we propose four schemes, with varying levels of complexity to cancel the ICI and ISI. These four schemes arise by considering different combinations of two choices:

- *Selection or Combining:* While demodulating subband  $m$ , we use samples from both arrays in the *combining* scheme. On the other hand, in the *selection* scheme, we only use the samples from the array that sees the stronger channel response. Specifically, denoting the channel response at array  $i$  by  $(p^{(i)}[0], p^{(i)}[1], \dots, p^{(i)}[v])$ , we choose samples from the array that has a larger value of  $\sum_{j=0}^v |p^{(i)}[j]|^2$ . The block diagrams of the selection schemes and combining schemes are shown in Figure 6.4 and Figure 6.5, respectively.

- *Independent or Joint:* In the *independent* mode, we treat the interference from subbands  $m - 1$  and  $m + 1$  as noise while designing an equalizer for subband  $m$ . In the *joint* mode, we exploit the structure of the interference from subbands  $m - 1$  and  $m + 1$  while designing the equalizer. We now explain the models for each of these schemes in detail.

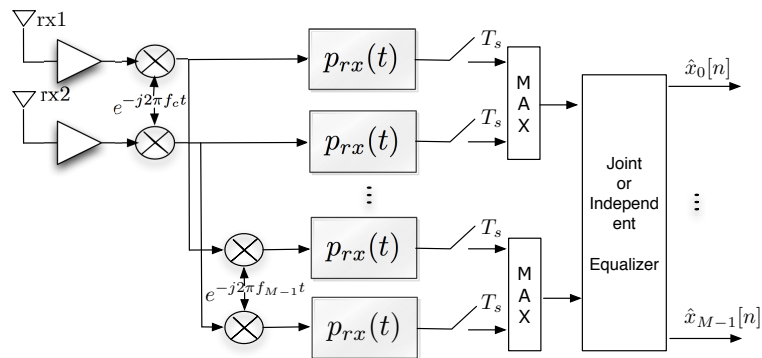


**Figure 6.4:** Block diagram of ISEL or JSEL scheme.

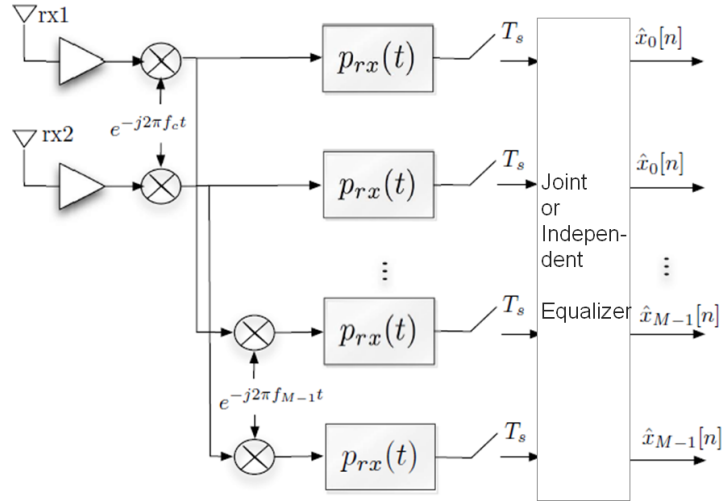


**Figure 6.5:** Block diagram of ICOM or JCOM scheme.

**Independent Selection scheme (ISEL):** Suppose that we are demodulating subband  $m$ . We use a superscript  $s$  to denote the samples and the channel matrices from the “selected” (or, “stronger”) array (as  $\mathbf{y}_m^s[n]$ ,  $\mathbf{H}_{m,m}^s$ ,  $\mathbf{H}_{m,m-1}^s$ ,  $\mathbf{H}_{m,m+1}^s$  respectively). Treating the interference from adjacent bands as noise in (6.12), we get the model

$$\mathbf{y}_m^s[n] = \mathbf{H}_{m,m}^s \mathbf{x}_m[n] + \mathbf{n}'_m[n], \quad (6.13)$$

where the noise covariance is given by:

$$\mathbf{C} = \mathbb{E} \left( \mathbf{n}'_m[n] \mathbf{n}'_m^H[n] \right) = \sigma^2 \mathbb{I} + \sigma_x^2 \mathbf{H}_{m,m-1}^s (\mathbf{H}_{m,m-1}^s)^H + \sigma_x^2 \mathbf{H}_{m,m+1}^s (\mathbf{H}_{m,m+1}^s)^H, \quad (6.14)$$

where  $\sigma^2 = N_0/2$  and  $\sigma_x^2$  denoting the transmit power in each symbol.

**Joint Selection scheme (JSEL):** In each of the subbands  $m - 1, m$  and  $m + 1$ , we choose samples from the antenna array that sees the stronger channel in the respective subband. In this case, we have the model

$$\begin{bmatrix} \mathbf{y}_{m-1}^s[n] \\ \mathbf{y}_m^s[n] \\ \mathbf{y}_{m+1}^s[n] \end{bmatrix} = G_{JS} \begin{bmatrix} \mathbf{x}_{m-1}[n] \\ \mathbf{x}_m[n] \\ \mathbf{x}_{m+1}[n] \end{bmatrix} + \begin{bmatrix} \mathbf{n}_{m-1}^s[n] \\ \mathbf{n}_m^s[n] \\ \mathbf{n}_{m+1}^s[n] \end{bmatrix}, \quad (6.15)$$

$$\text{where } G_{JS} = \begin{bmatrix} \mathbf{H}_{m-1,m-1}^s & \mathbf{H}_{m-1,m}^s & \mathbf{0} \\ \mathbf{H}_{m,m-1}^s & \mathbf{H}_{m,m}^s & \mathbf{H}_{m,m+1}^s \\ \mathbf{0} & \mathbf{H}_{m+1,m}^s & \mathbf{H}_{m+1,m+1}^s \end{bmatrix}.$$

Note that we are ignoring the contributions to  $\mathbf{y}_{m-1}^s[n]$  and  $\mathbf{y}_{m+1}^s[n]$  from the transmissions in the  $m - 2^{th}$  and  $m + 2^{th}$  subbands respectively.

**Independent Combining scheme (ICOM):** We use samples from subband  $m$  from both the arrays, but treat the interference from subbands  $m - 1$  and  $m + 1$  as noise. We use the superscript  $(i)$  to denote the samples collected from array  $i$  and the channel matrix seen by array  $i$ . Thus, we have the model

$$\begin{bmatrix} \mathbf{y}_m^{(1)}[n] \\ \mathbf{y}_m^{(2)}[n] \end{bmatrix} = \begin{bmatrix} \mathbf{H}_{m,m}^{(1)} \\ \mathbf{H}_{m,m}^{(2)} \end{bmatrix} \mathbf{x}_m[n] + \begin{bmatrix} \boldsymbol{\eta}_m^{(1)} \\ \boldsymbol{\eta}_m^{(2)} \end{bmatrix}, \quad (6.16)$$

where

$$\begin{bmatrix} \boldsymbol{\eta}_m^{(1)} \\ \boldsymbol{\eta}_m^{(2)} \end{bmatrix} = \mathbf{K}_{m-1} \mathbf{x}_{m-1}[n] + \mathbf{K}_{m+1} \mathbf{x}_{m+1}[n] + \begin{bmatrix} \mathbf{n}_m^{(1)}[n] \\ \mathbf{n}_m^{(2)}[n] \end{bmatrix},$$

and  $\mathbf{K}_{m-1}$  stacks  $\mathbf{H}_{m,m-1}^{(1)}$  above  $\mathbf{H}_{m,m-1}^{(2)}$  and  $\mathbf{K}_{m+1}$  stacks  $\mathbf{H}_{m,m+1}^{(1)}$  above  $\mathbf{H}_{m,m+1}^{(2)}$ .

From this equation, we obtain the covariance of the noise to be:

$$\mathbf{C} = \sigma_x^2 (\mathbf{K}_{m-1} \mathbf{K}_{m-1}^H + \mathbf{K}_{m+1} \mathbf{K}_{m+1}^H) + \sigma^2 \mathbb{I}. \quad (6.17)$$

**Joint Combining scheme (JCOM):** We use all the available information (samples from both arrays from subbands  $m - 1, m$  and  $m + 1$ ) while demodulating subband  $m$ , giving us the model

$$\begin{bmatrix} \mathbf{y}_{m-1}^{(1)}[n] \\ \mathbf{y}_{m-1}^{(2)}[n] \\ \mathbf{y}_m^{(1)}[n] \\ \mathbf{y}_m^{(2)}[n] \\ \mathbf{y}_{m+1}^{(1)}[n] \\ \mathbf{y}_{m+1}^{(2)}[n] \end{bmatrix} = G_{JC} \begin{bmatrix} \mathbf{x}_{m-1}[n] \\ \mathbf{x}_m[n] \\ \mathbf{x}_{m+1}[n] \end{bmatrix} + \begin{bmatrix} \mathbf{n}_{m-1}^{(1)}[n] \\ \mathbf{n}_{m-1}^{(2)}[n] \\ \mathbf{n}_m^{(1)}[n] \\ \mathbf{n}_m^{(2)}[n] \\ \mathbf{n}_{m+1}^{(1)}[n] \\ \mathbf{n}_{m+1}^{(2)}[n] \end{bmatrix}, \quad (6.18)$$

$$\text{where } G_{JC} = \begin{bmatrix} \mathbf{H}_{m-1,m-1}^{(1)} & \mathbf{H}_{m-1,m}^{(1)} & \mathbf{0} \\ \mathbf{H}_{m-1,m-1}^{(2)} & \mathbf{H}_{m-1,m}^{(2)} & \mathbf{0} \\ \mathbf{H}_{m,m-1}^{(1)} & \mathbf{H}_{m,m}^{(1)} & \mathbf{H}_{m,m+1}^{(1)} \\ \mathbf{H}_{m,m-1}^{(2)} & \mathbf{H}_{m,m}^{(2)} & \mathbf{H}_{m,m+1}^{(2)} \\ \mathbf{0} & \mathbf{H}_{m+1,m}^{(1)} & \mathbf{H}_{m+1,m+1}^{(1)} \\ \mathbf{0} & \mathbf{H}_{m+1,m}^{(2)} & \mathbf{H}_{m+1,m+1}^{(2)} \end{bmatrix}.$$

In all these cases, the general model we have is

$$\mathbf{Y} = \mathbf{U}\mathbf{s} + \mathbf{n} \quad (6.19)$$

where the noise  $\mathbf{n}$  has a covariance matrix  $\mathbf{C}$ , including both the complex Gaussian thermal noise and the interference signal. Let us denote the entries of  $\mathbf{s}$  by  $(s_0, s_1, s_2, \dots)$  and suppose that we wish to estimate  $s_0$ . Denoting the corresponding columns of  $\mathbf{U}$  by  $\{\mathbf{u}_i\}$ , we can rewrite the model in (6.19) as

$$\mathbf{Y} = s_0\mathbf{u}_0 + \sum_{i \neq 0} s_i\mathbf{u}_i + \mathbf{n}. \quad (6.20)$$

The MMSE estimate of  $s_0$  is given by [48]

$$\hat{s}_0 = \mathbf{w}^H \mathbf{Y} = (\mathbf{R}^{-1} \mathbf{p})^H \mathbf{Y}, \quad (6.21)$$

where  $\mathbf{R} = E\{\mathbf{Y}\mathbf{Y}^H\} = \sigma_x^2 \mathbf{U}\mathbf{U}^H + \mathbf{C}$  and  $\mathbf{p} = E\{s_0^* \mathbf{Y}\} = \sigma_x^2 \mathbf{u}_0$ . The effective SINR at the output of the equalizer is given by

$$\text{SINR} = \frac{E_s}{E_i + E_n} = \frac{\sigma_x^2 |\mathbf{w}^H \mathbf{u}_0|^2}{\sigma_x^2 \sum_{i \neq 0} |\mathbf{w}^H \mathbf{u}_i|^2 + \mathbf{w}^H \mathbf{C} \mathbf{w}} \quad (6.22)$$

where  $E_s$  denotes the effective signal power,  $E_i$  denotes the residual interference power and  $E_n$  represents the effective remaining noise power. We can use this effective SINR to compute the bit error rate in our following simulation results.

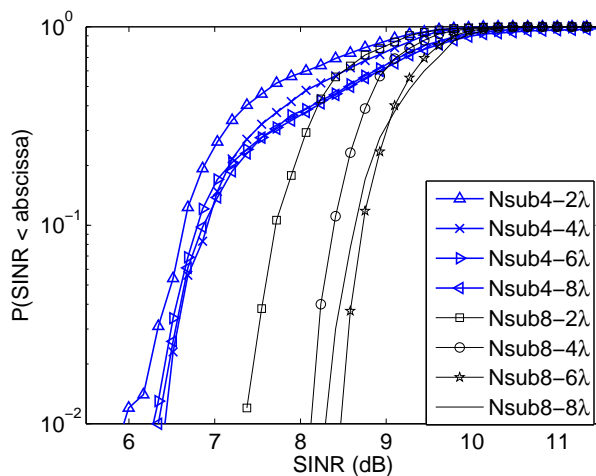


**Figure 6.6:** The CDF of the obtained SINR of the ISEL scheme with 4 and 8 subband channels for different antenna separations from  $2\lambda$  to  $8\lambda$ .

## 6.4 Simulation Results

We simulate links with a range of 200m and a bandwidth of 2 GHz. We consider the three-ray channel model from Section 2.3: one reflection each off a nearby wall and street in addition to the LoS path. As before, the distance to the wall  $r_{wall}$  is uniformly distributed in [4m, 20m] and the distance to the street is uniformly distributed in [5m, 8m]. The reflections result in a maximum delay spread of 13ns (26 symbol periods). We choose smooth wood and concrete as the reflection surfaces for the street and the wall respectively, whose dielectric parameters are given in Section 2.2.2. We use square root raised cosine filters at the transmitter and the receiver with rolloff factors of 0.2. We split the transmissions into either

4 or 8 subbands and use QPSK modulation in each band with the receive SNR along the LoS path being 11 dB.

### 6.4.1 Selecting the Number of Subbands

An OFDM system converts a vector channel into many scalar channel by employing sufficient number of subcarriers (subbands) such that the channel delay spread is much smaller than the symbol period for each sub-band and hence inducing one-tap channel impulse response (CIR). However, since increasing the number of subchannels in our system directly increases the number of required RF chains and hence the complexity of the RF front end, it is essential to find a reasonably moderate number of subbands that achieve the desired reduction in ADC sampling rate, while requiring a small number of equalizer taps and hence reducing the dynamic range.

**Two-ray channel model:** We evaluate how the number of channel taps depends on the number of subbands for the two-ray channel model including the LoS and the wall reflection. We neglect the inter-carrier interference (ICI) to get an analytical handle. The normalized two-ray channel model in the frequency domain is given by:

$$H_{2ray}(f) = 1 + \alpha_1 e^{j\theta_1} e^{-j2\pi f\tau_1},$$

where  $\tau_1$  denotes the delay of the wall reflected ray relative to the LoS path (similar to  $\tau_i$  in (2.6)), the relative phase  $\theta_1$  is assumed to be uniform within  $[0, 2\pi]$ ,  $f \in [-\frac{B}{2}, \frac{B}{2}]$  for the fullband channel ( $B$  denotes channel bandwidth) and  $f \in [-\frac{B}{2M}, \frac{B}{2M}]$  for the system with  $M$  subbands.

We now perform a series of simplifying assumptions: the Nyquist sampling rate is employed with perfect timing synchronization and the delay spread  $\tau_1 = kM/B$ , where  $k$  is an integer. This results in a single tap for the channel impulse response for both the LoS and the wall reflection. Under these assumptions, we consider the CIR length for the following two extreme conditions:

1. When the delay spread is significantly larger than the subband symbol period ( $k \gg 1$ ), the CIR length for the fullband channel and the subband channel are  $kM$  and  $k$ , respectively, which means the CIR length decreases linearly with increasing number of subbands.
2. When the delay spread is close to or smaller than the subband symbol period ( $k \approx 1$ ), the two taps of the reflected ray and the LoS ray cannot be distinguished, which means further increasing the number of subbands cannot significantly reduce the CIR length.

Figure 6.7 plots the time domain channel impulse responses, including channel taps up to 20 dB lower than the strongest channel tap, for a system with different numbers of subbands, where we choose  $B = 2$  GHz and  $r_{wall} = 22.04$  m, corresponding to  $\tau_1 = 16$  ns ( $32/B$ ). As we can see from this figure, the simulation results match with our previous claims about the dependence of the CIR length on the number of subbands. First, when  $\tau_1 = 16ns > 4/B = 8ns$ , the number of channel taps decreases from 34 in the fullband system to 10 in the 4 subband system, where  $34/10 \approx 3.4$  is slightly smaller than the number of subbands 4. This is mainly caused by the violation of Nyquist sampling rate and hence the resultant ISI. Second, when  $\tau_1 = 16ns < 16/B = 32ns$ , the number of channel taps only decreases from 6 in the 8 subband system to 4 in the 16 subband system. We further show that the same trends hold for the three-ray channel model in the following discussion.

**Three-ray channel model:** In Figure 6.8, we plot the time domain CIR for the three-ray channel model including the LoS ray, the reflected rays from the nearby wall and the ground, where we set  $r_{wall} = 22.04$ m and  $r_{street} = 5$  m, contributing to relative delays of 16 ns and 0.83 ns, respectively. Similar to the result for the two-ray model, we observe from Figure 6.8 that the CIR length roughly scales down linearly with increasing number of subbands when  $\tau_{max} \gg M/B$  and the CIR length only decreases by a small amount when  $\tau_{max} \sim M/B$  (scales down

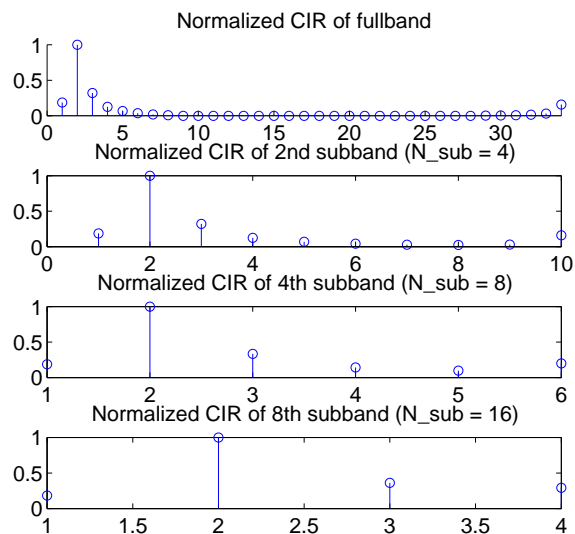


**Figure 6.7:** Illustration of normalized channel impulse responses for the two-ray channel model in a system with different numbers of subbands.

$11/5 = 2.2$  times from the 4 subband system to 16 subband system), where  $\tau_{max}$  is the maximum delay spread for the system with a given subband number.

Therefore, we focus on the relatively small number of subbands 4 or 8 in this dissertation that significantly reduces the CIR length compared to the fullband system, thereby leading to the low complexity RF front end. Although our previous observations about the CIR length neglected ICI, when we consider the channel taps up to 20 dB below the highest channel tap, we observe that the CIR length still remains the same after including ICI. This is because the channel taps of ICI are more than 20 dB smaller than the highest channel tap. Therefore, our

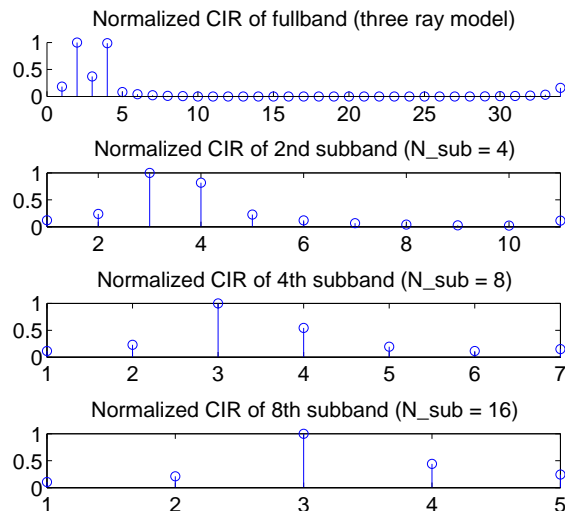


**Figure 6.8:** Illustration of normalized channel impulse responses for the three-ray channel model in a system with different numbers of subbands.

previous conclusions on how to select the appropriate number of subbands still hold even if the ICI effect is considered.

### 6.4.2 Design of Multiple Antenna Arrays

**Array separation:** We investigate the performance of the ISEL scheme with varying distances between the receive arrays with the goal of choosing a “good” value for the array separation. We have shown in Section 3.3.3 that spatial diversity with an antenna spacing of several wavelengths successfully overcomes fading and provides quasi-deterministic diversity performance. Therefore, we consider two arrays separated by  $2\lambda - 8\lambda$  (in both the horizontal and vertical directions).

We use the ISEL scheme with 21 equalizer taps and plot the CDF of the SINR from (6.22) in Figure 6.6. For 4-subband transmission, we see that the performance with array separations of  $4\lambda$ ,  $6\lambda$  and  $8\lambda$  are nearly identical. Similarly, for 8-subband transmission, array separations of  $6\lambda$  and  $8\lambda$  work well. In the following simulations, we set the array separation to be  $6\lambda$  (in both directions) since it works well with both 4 and 8-subband transmissions.

**Performance trends:** We investigate the SINR at the output of the equalizer for different schemes as function of the number of equalizer taps per subband per array, which we denote by  $N_{taps}$ . Thus, the total number of equalizer taps for JCOM, JSEL, ICOM, ISEL are  $6N_{taps}$ ,  $3N_{taps}$ ,  $2N_{taps}$ , and  $N_{taps}$  respectively. We consider a scenario with a large delay spread ( $r_{wall} = 20$  m and  $r_{street} = 8$  m) and assume that the channel is known perfectly. We average the SINR from (6.22) over all the subbands, except for the ones at the edges (bands 2 and 3 for the 4-subband system; bands 2-7 for the 8 subband system). We plot the results in Figure 6.9 and make the following observations:

- The performance with 8 subbands is significantly better than that with 4 subbands for the ICOM, JSEL and ISEL schemes (for JCOM, the performance is similar when the number of equalizer taps is large). Of course, we need twice as many equalizers for the 8-subband transmission when compared to 4-subband transmission.

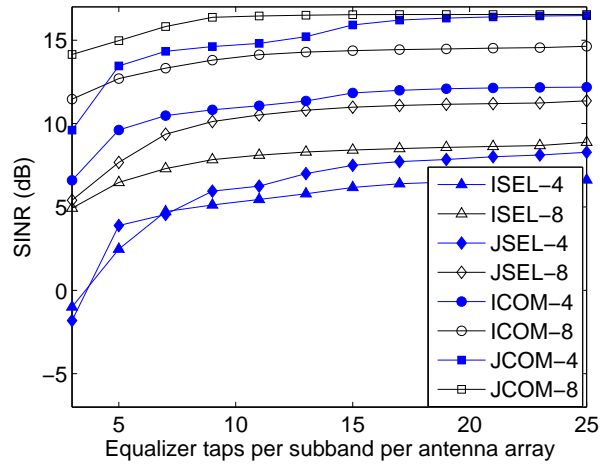


**Figure 6.9:** SINR as a function of equalizer taps per subband per antenna array for four schemes with 4 subbands and 8 subbands.

- The SINR achieved with ICOM is 4 dB higher than that with JSEL even though it uses *fewer* equalizer taps than JSEL ( $2N_{taps}$  vs.  $3N_{taps}$ ). Thus, it is essential to combine signals from both arrays, rather than to simply select the stronger one, to combat frequency selective fading and ICI.

- In terms of the SINR achieved with a large number of equalizer taps, we can rank the schemes as  $JCOM > ICOM > JSEL > ISEL$  with the ratios of their complexities being 6 : 2 : 3 : 1.

### 6.4.3 BER Performance

We investigate the performance of the different schemes when the channels are not known perfectly and the equalizer taps are estimated from a training sequence.

We compute the equalizer taps in the  $m$ th subband by adaptively estimating  $\mathbf{R}_m$  and  $\mathbf{p}_m$  as  $\mathbf{R}_m = \frac{1}{N_{train}} \sum_i^{N_{train}} \mathbf{Y}_m[i] \mathbf{Y}_m^H[i]$  and  $\mathbf{p}_m = \frac{1}{N_{train}} \sum_i^{N_{train}} \mathbf{Y}_m[i] x_m^*[i]$  from training symbols  $\{x_m[i], i = 1, 2, \dots, N_{train}\}$  and then using them in (6.21). We simulate the performance by transmitting  $10^5$  symbols of which 1000 symbols are used for training. We use 21 equalizer taps per subband per antenna array and consider 100 channel realizations with different distances to the wall  $r_{wall}$  and the street  $r_{street}$ . We plot the average BER from simulations in the 4th subband of the 8-subband system in Figure 6.10. We also plot the BER assuming perfect channel knowledge  $Q(\sqrt{\text{SINR}})$ , where the SINR is given by (6.22). We make the following observations:

- Both ISEL and JSEL have relatively high error floors ( $8 \times 10^{-3}$  and  $5 \times 10^{-5}$  at 14 dB respectively). This happens because a finite length MMSE equalizer operating on symbol-rate samples does not have sufficient dimensions to suppress the ISI completely (even ignoring ICI) [48]. On the other hand, using samples from both arrays in ICOM and JCOM essentially provides a fractionally spaced equalizer with sufficient degrees of freedom to suppress interference completely, thereby eliminating the error floor. We further verify these results by comparing the BER performance between ISEL with a small oversampling factor (defined as the ratio between the sampling rate and the symbol rate) and the ICOM scheme with Nyquist sampling.

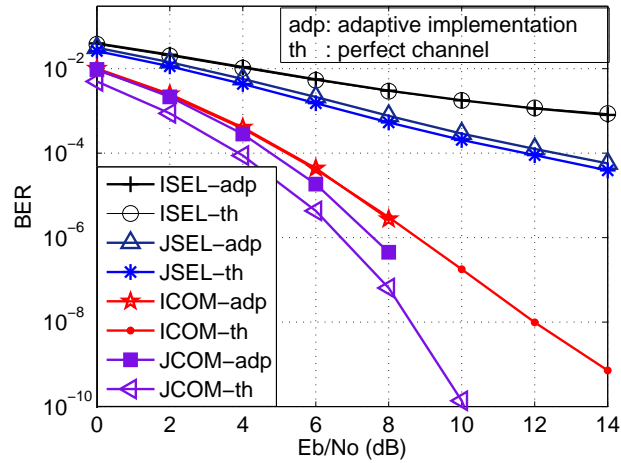


**Figure 6.10:** BER as a function of  $E_b/N_0$  (along the LoS path) for different schemes with both adaptive implementation and calculation using perfect channel knowledge.

- Comparing the combining strategies (the adaptive implementation curves), we see that JCOM provides a 1 dB gain over ICOM (at  $E_b/N_0 = 8$  dB), while incurring thrice the complexity.
- With JCOM and JSEL, we have to estimate a larger number of equalizer taps in comparison to ICOM and ISEL. The errors in estimating the equalizer taps result in a slightly larger BER than predictions assuming perfect channel knowledge. We see that the simulated performance is about 0.4 dB and 0.9 dB worse than the theoretical prediction for JSEL and JCOM respectively.

**The influence of oversampling on the BER performance:** We have shown that the combining scheme (ICOM or JCOM) yields much better BER perfor-

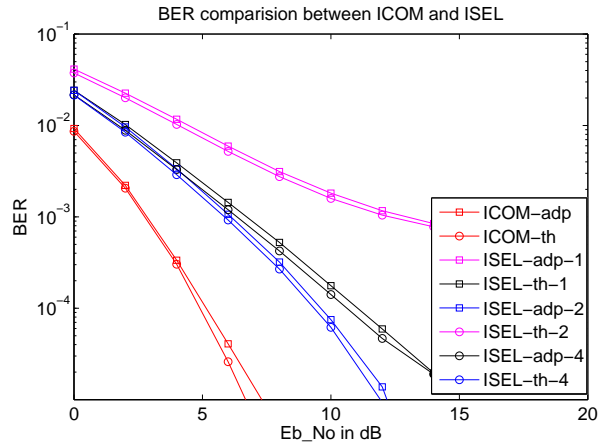


**Figure 6.11:** BER comparison between the ICOM scheme with Nyquist sampling and ISEL scheme with oversampling factors of 1, 2 and 4. (adp: adaptive implementation, th: calculation using perfect channel knowledge)

mance relative to the selective scheme (ISEL or JSEL), possibly because it is equivalent to the fractionally spaced equalizer (compared to the symbol-spaced equalizer for ISEL or JSEL). Thus, an interesting topic to investigate is the impact of the oversampling factor on the BER performance for the selective scheme. Although our aim is to reduce the ADC sampling rate, it is still worth to study whether a relatively small oversampling factor can significantly improve the BER performance for the selective scheme such that its performance becomes comparable to that of the combining scheme.

Figure 6.11 shows that BER significantly reduces for the ISEL scheme as the oversampling factor increases from 1 to 2 and 4. For example, BERs of  $1 \times 10^{-3}$ ,  $5.9 \times 10^{-5}$  and  $1.4 \times 10^{-5}$  are achieved at  $E_b/N_0$  of 12 dB with the oversampling

factors of 1, 2 and 4, respectively. However, the BER achieved by the ICOM scheme with Nyquist sampling rate still exhibits much better performance compared to the ISEL scheme with the oversampling factor of 2 or 4. In particular, we have the following observations:

- When noise power is more dominant than the interference power ( $E_b/N_0$  is small), the required  $E_b/N_0$ , to achieve the same BER, for the ICOM scheme is about 2 dB smaller than that for the ISEL scheme with an oversampling factor of 2. For example, the ICOM scheme achieves BER of  $1 \times 10^{-2}$  at  $E_b/N_0$  of 0 dB, while the ISEL with an oversampling factor of 2 achieves the same BER at  $E_b/N_0$  of 2.2 dB. Note that, given the same noise power, the combining scheme should achieve a 3 dB higher effective signal power  $E_b$  compared to the selective scheme if both of the two received signals experience the same channel impulse responses. Since, for the selective scheme, we choose the array seeing the stronger channel, we expect that the ICOM scheme (combining the signals from both the stronger channel and the weaker channel) achieves the similar performance with a smaller  $E_b/N_0$  (less than 3 dB difference) relative to the ISEL scheme.
- As  $E_b/N_0$  increases (the interference becomes more dominant relative to noise), the gap between ICOM and ISEL with an oversampling factor of 2

or 4 increases significantly, such as a gap of 5 dB exists at BER of  $3 \times 10^{-4}$  (corresponding to  $E_b/N_0$  of 9 dB and 4 dB for ISEL with an oversampling factor of 2 and ICOM, respectively). That is spatial diversity achieved by the ICOM scheme appears to also reduce the noise enhancement due to linear suppression of ICI and ISI.

## 6.5 Summary

Analog Multitone is a general technique for scaling communication systems to large bandwidths while sidestepping the ADC bottleneck. In this work, we have shown that it can be used in conjunction with beamforming and spatial diversity for robustly attaining multiGigabit rates on outdoor 60 GHz links. Separate linear equalization for each subband suffices to avoid performance floors, as long as the additional degrees of freedom provided by using samples from both receive arrays are used (i.e., the ICOM scheme provides perhaps the best complexity/performance tradeoff among the schemes considered here). Interesting topics for future investigation include exploring potential performance gains from decision feedback, and more intelligent beamforming (e.g., MMSE adaptation for multipath combining and suppression).

# Chapter 7

## Conclusions

Our investigation shows that the sparse multipath channels associated with highly directional mm wave links are fundamentally different from the rich scattering channels at lower carrier frequencies, in terms of both achievable performance (quasi-deterministic guarantees) and design rules of thumb. For spatial diversity, the antennas need to be spaced by multiple wavelengths (feasible with compact form factors at the small wavelengths of interest to us); for frequency diversity, the minimum delay spread (the delay of the first reflected path relative to the LoS path) rather than the rms delay spread is the relevant parameter.

We have studied different equalizer strategies for the AMT scheme in a  $1 \times 2$  SIMO system. Our results show that utilizing beamforming and spatial diversity in conjunction with AMT scheme successfully provides robust multiGigabit transmission rates on outdoor 60 GHz links while sidestepping the ADC bottleneck. We can also conclude that individually linear equalization for each subband suf-

fices to avoid BER performance floor, as long as the additional freedom provided by samples from both receive arrays are used.

Future work includes the potential performance gains from more sophisticated beamforming strategies, particularly with very large arrays [49], and the investigation of diversity/multiplexing tradeoffs for sparse multipath channels (spatial multiplexing with compact form factors becomes feasible at the ranges of interest to us for carrier frequencies beyond 100 GHz).

# Bibliography

- [1] M. Luise, F. Giannetti, and R. Reggiannini, “Mobile and personal communications in the 60 GHz Band: a survey,” *Wireless Personal Communications*, vol. 10, no. 2, pp. 207-243, 1999.
- [2] A. Siligaris, O. Richard, and et al., “A 65-nm CMOS Fully Integrated Transceiver Module for 60-GHz Wireless HD Applications,” *IEEE Journal of Solid-State Circuits*, vol. 46, no. 12, pp. 3005-3017, 2011.
- [3] K. Okada, N. Li, and et al., “A 60-GHz 16QAM/8PSK/QPSK/BPSK Direct-Conversion Transceiver for IEEE802. 15.3 c,” *IEEE Journal of Solid-State Circuits*, vol. 46, no. 12, pp. 2988-3004, 2011.
- [4] <http://wirelessgigabitalliance.org>, January 2010.
- [5] IEEE P802.11 TASK GROUP AD, [http://www.ieee802.org/11/Reports/tgad\\_update.htm](http://www.ieee802.org/11/Reports/tgad_update.htm).
- [6] R. Mudumbai, S. Singh, and U. Madhow, “Medium access control for 60 GHz outdoor mesh networks with highly directional links,” in *Proc. IEEE INFOCOM 2009, Mini Conference*, Apr. 2009, pp. 2871-2875.
- [7] S. Singh, R. Mudumbai and U. Madhow, “Distributed Coordination with Deaf Neighbors: Efficient Medium Access for 60 GHz Mesh Networks ,” in *Proc. IEEE INFOCOM 2010*, San Diego, CA, March 2010.
- [8] M.-S. Choi, G. Grosskopf, and D. Rohde, “Statistical Characteristics of 60 GHz wideband indoor propagation channel,” *Proc. IEEE PIMRC 2005*, vol. 1, pp. 599-603, Sept. 2005.
- [9] N. Moraitis and P. Constantinou, “Indoor channel measurements and characterization at 60 GHz for wireless local area network applications,” *IEEE Trans. Antennas Propag.*, vol. 52, no. 12, pp. 3180-3189, Dec. 2004.

- [10] H. Xu, V. Kukshya, and T. S. Rappaport, "Spatial and temporal characteristics of 60-GHz indoor channels," *IEEE J. Select. Areas Commun.*, vol. 20, no. 3, pp. 620-630, Apr. 2002.
- [11] S. Geng, J. Kivinen, X. Zhao, and P. Vainikainen, "Millimeter-Wave Propagation Channel Characterization for Short-Range Wireless Communications." *IEEE Vehicular Tech.*, vol. 58, no. 1, pp. 3-13, Jan. 2009.
- [12] D. M. Matic, H. Harada, R. Prasad, "Indoor and outdoor frequency measurements for MM-waves in the range of 60 GHz," *Proceedings IEEE 48th Vehicular Technology Conference*, Ottawa, Canada, May 1998, vol. 1, pp. 567-571.
- [13] L. M. Correia and P. O. Frances, "A propagation model for the estimation of the average received power in an outdoor environment in the millimeter waveband," in *Proc. VTC*, vol. 3, June 1994, pp. 1785-1788.
- [14] A. Plattner, N. Prediger, W. Herzig, "Indoor and outdoor propagation measurements at 5 and 60 GHz for radio LAN application," Internal Report, DASA, Ulm, Germany.
- [15] L.M. Correia and J.R. Reis. "Wideband characterisation of the propagation channel for outdoors at 60 GHz." In *Proceedings of IEEE International Symposium on Personal, Indoor and Mobile Radio Commun.*, vol. 2, pp 752-755, Oct. 1996.
- [16] LØvnes, G., Reis, J. J., and Rækken, R. H. "Channel sounding measurements at 59 GHz in city streets." *5th IEEE Int. Symp. on Personal, Indoor and Mobile Radio Communications*, The Hague, The Netherlands, September 1994.
- [17] S. Singh, F. Ziliotto, and et all., "Blockage and Directivity in 60 GHz Wireless Personal Area Networks: From Cross-Layer Model to Multihop MAC Design," *IEEE JSAC, Special Issue on Realizing Gbps Wireless Personal Area Networks*, 2009.
- [18] S. Hur, T. Kim, D. Love, etc "Multilevel millimeter wave beamforming for wireless backhaul," in *Proc. 2nd Globecom Workshop on Femtocell Networks 2011*, Dec. 2011.
- [19] D. J. Love, "Wireless backhaul (and access) at millimeter wave frequencies," in *IEEE Communication Theory Workshop 2012*, May. 2012.

- [20] E. Torkildson, C. Sheldon, U. Madhow, M. Rodwell, “Nonuniform array design for robust millimeter-Wave MIMO links”, in *Proc. IEEE Global Communications Conference 2009 (Globecom)*, Honolulu, Hawaii, November 2009.
- [21] C. Sheldon, M. Seo, E. Torkildson, M. Rodwell, and U. Madhow, “Four-Channel Spatial Multiplexing Over a Millimeter-Wave Line-of-Sight Link,” *MTTS International Microwave Symposium*, Boston, Massachusetts, June 2009.
- [22] E. Torkildson, U. Madhow, M. Rodwell, “Indoor millimeter wave MIMO: feasibility and performance,” *IEEE Transactions on Wireless Communications*.
- [23] H. Zhang, S. Venkateswaran, and U. Madhow. “Channel modeling and MIMO capacity for outdoor millimeter wave links.” in *Proc. IEEE WCNC 2010*, Apr. 2010.
- [24] H. Zhang and U. Madhow. “Statistical modeling of fading and diversity for outdoor 60 GHz channels.” in *Proc. International Workshop on mmWave Communications (mmCom10)*, 2010.
- [25] E. Torkildson, H. Zhang, U. Madhow, “Channel Modeling for Millimeter Wave MIMO,” *Information Theory and Applications Workshop(ITA)*, San Diego, CA, Feb. 2010.
- [26] H. Zhang and U. Madhow. “Quasi-deterministic diversity for sparse multipath channels: design of robust, highly directional, outdoor 60 GHz links”, *IEEE Transactions on Wireless Communications (submitted)*
- [27] H. Zhang, S. Venkateswaran and U. Madhow, “Analog Multitone with Interference Suppression: Relieving the ADC Bottleneck for Wideband 60 GHz Systems,” *IEEE Globecom*, to be appeared, Dec. 2012.
- [28] B. Le, T.W. Rondeau, J.H. Reed, and C.W. Bostian “Analog-to-digital converters,” *IEEE Signal Processing Magazine*, 22(6):69–77, 2005.
- [29] S. Ponnuru, M. Seo, U. Madhow, and M. Rodwell “Joint mismatch and channel compensation for high-speed OFDM receivers with time-interleaved ADCs.” *IEEE Transactions on Communications*,58(8):2391–2405,2010.
- [30] Orfanidis, S. J., “Electromagnetic Waves and Antennas,” Rutgers University, 2008.

- [31] J. D. Kraus and R. J. Marhefka. “Antennas: for All Applications,” 3rd Ed. McGraw-Hill, New York, 2002.
- [32] S.K. Yong and C.-C. Chong, “An overview of multigigabit wireless through millimeter wave technology: potentials and technical challenges,” *EURASIP Journal on Wireless Communications and Networking*, vol. 2007.
- [33] V. Kvicera and M. Grabner, “Rain Attenuation at 58 GHz: Prediction versus Long-Term Trial Results,” in *Proc. EURASIP J. Wireless Commun. Netw.* 2007
- [34] T. Yao, M. Gordon, K.K.W Tang, etc. “Algorithmic Design of CMOS LNAs and PAs for 60-GHz Radio,” *IEEE J. Solid-State Circuits*, vol. 42, no.5, pp. 1044-1057, May 2007.
- [35] P. F. M. Smulders, “Deterministic modelling of indoor radio propagation at 40-60 GHz,” *Wireless Pers. Commun.*, vol. 1, no. 2, pp. 127-135, Jun. 1994.
- [36] L. M. Correia and P. O. Françês, “Estimation of materials characteristics from power measurements at 60 GHz,” in *Proc. IEEE 7th Int. Conf. Personal, Indoor, and Mobile Radio Commun.*, vol. 1, Oct. 1994, pp. 510-513.
- [37] K. Sato, T. Manabe, J. Polivka, T. Ihara, Y. Kasashima, and K. Yamaki, “Measurement of the complex refractive index of concrete at 57.5 GHz,” *IEEE Trans. Antennas Propagat.*, vol. 44, pp. 35-40, Jan. 1996.
- [38] B. Langen, G. Lober, and W. Herzig, “Reflection and transmission behavior of building materials at 60 GHz,” in *Proc. IEEE PIMRC’94*, Hague, Netherlands, pp. 505-509. Sept. 1994.
- [39] A. Goldsmith, “*Wireless Communications.*” Cambridge Univ. Press, 2005 Cambridge, U.K.
- [40] A. M. Hammoudeh, M. G. Sánchez, and E. Grindrod, “Experimental analysis of propagation at 62 GHz in suburban mobile radio microcells,” *IEEE Trans. on Vehicular Technology*, vol. 48, no. 2, pp 576-588, Mar. 1999.
- [41] D. N. C. Tse and P. Viswanath, “*Fundamentals of Wireless Communications*”. Cambridge University Press, 2005.
- [42] A. Amirkhany, V. Stojanovic, and M. Horowitz. “Multi-tone signaling for high-speed backplane electrical links.” in *Proc. IEEE GLOBECOM’ 04*, volume 2, 2004.

- [43] A. Amirkhany, A. Abbasfar, , and et al., “A 24 Gb/s software programmable analog multi-tone transmitter.” *IEEE Journal of Solid-State Circuits*, 43(4):999–1009, 2008.
- [44] W. Namgoong. “A channelized digital ultrawideband receiver.” *IEEE Transactions on Wireless Communications*, 2(3):502–510, 2003.
- [45] P. Amini, R. Kempter, and B. Farhang-Boroujeny. “A comparison of alternative filterbank multicarrier methods for cognitive radio systems.” in *Software Defined Radio Technical Conference*, 2006.
- [46] M. Park and P. Gopalakrishnan. “Analysis on spatial reuse and interference in 60-GHz wireless networks” *IEEE Journal on Selected Areas in Communications*, 2009.
- [47] J. Akkermans and M. Herben. “Planar beam-forming array for broadband communication in the 60 GHz band.” in *The Second European Conference on Antennas and Propagation, EuCAP 2007*, IET, 2007.
- [48] U. Madhow. “*Fundamentals of Digital Communication*”. Cambridge University Press, 2008.
- [49] D. Ramasamy, S. Venkateswaran and U. Madhow. “Compressive adaptation of large steerable arrays,” *ITA Workshop* pp. 234 -239, Feb. 2012.